Ceramics International 51 (2025) 55341–55354

Contents lists available at ScienceDirect

Ceramics International

journal homepage: www.elsevier.com/locate/ceramint

Effect of sintering temperature on structural, microstructural, and dielectric properties of $(Co_{0.2}Fe_{0.2}Ni_{0.2}Al_{0.2}Ti_{0.2})_3O_4$ multi-cations high entropy oxides

Rajesh K. Mishra [a,*], F.B. Minussi [b,**], Priyanka Kumari [c], Rohit R. Shahi [c,***], R.P. Yadav [d], Franziska Emmerling [a], E.B. Araújo [b,****]

[a] Department of Materials Chemistry, Federal Institute for Materials Research and Testing (BAM), Richard-Willstätter-Strasse 11, 12489, Berlin, Germany
[b] Department of Physics and Chemistry, São Paulo State University, Ilha Solteira, São Paulo, 15385-000, Brazil
[c] FMRL, Department of Physics, Central University of South Bihar, Gaya, 824236, India
[d] Department of Physics, Allahabad Degree College (University of Allahabad), 211003, India

ARTICLE INFO

Handling editor: P. Vincenzini

Keywords:
Multi-cations high entropy oxide
Mechanochemistry
Spinel structure
Fractal and impedance spectroscopic analysis

ABSTRACT

The study reports the effect of sintering temperature on structural, microstructural, and dielectric properties of $(Co_{0.2}Fe_{0.2}Ni_{0.2}Al_{0.2}Ti_{0.2})_3O_4$ spinel high-entropy oxides (HEOs) synthesized through the solid-state mechanochemistry method. The sintering of the ceramic powders was accomplished at three different temperatures (1000 °C, 1100 °C, and 1250 °C), followed by air quenching. XRD analysis along with Le-Bail refinement confirms that 1100 °C and 1250 °C sintered oxides comprised of a single cubic spinel phase ($Fd\bar{3}m$), while 1000 °C sintered oxide contains constituent oxides and a spinel phase. The phase formation of oxides sintered at 1100 °C and 1250 °C has also been confirmed by Raman spectroscopic analysis. Microstructural analysis revealed that the aggregated particle size increases with the rise in sintering temperature. With the change in sintering temperature, the dielectric behavior of the ceramic changed extensively. The 1100 °C sintered ceramic exhibits high frequency-dependent behavior, whereas the 1250 °C sintered ceramic yields low frequency-dependent behavior. The 1250 °C sintered HEO exhibits low-loss tangent ($\tan\delta = 0.01$) with higher dielectric permittivity ($\varepsilon' = 44$) at high frequency (1 MHz) compared to the 1100 °C sintered ceramic and many other conventional dielectrics. Fractal concept and impedance analysis have been employed to correlate the microstructure-dielectric property relation of $(Co_{0.2}Fe_{0.2}Ni_{0.2}Al_{0.2}Ti_{0.2})_3O_4$ spinel HEOs. The found Hurst exponent values for both different temperature-sintered HEOs are less than 0.5, indicating the anti-persistent behavior. This signifies that the height variations at neighboring pixels are negatively correlated. The present work is of fundamental importance in employing fractal analysis for the first time on spinel HEOs and correlating their properties. It also shows that processing conditions can effectively tailor the dielectric properties of the materials.

1. Introduction

Developing advanced ceramic materials has always been a vibrant opportunity to tackle the limitations of conventional ceramics used in different functional materials applications. The recent emergence of the high entropy approach has paved the way for researchers to design compositions with tailored functional properties [1–5]. The multi-elemental characteristics and distinct design strategy of the high entropy ceramics (HECs) open a new era of ceramics for advanced functional engineering applications [1–5]. Literature data imply that various HECs, such as high entropy oxides, high entropy carbides, high entropy borides, etc., have been reported and studied for multiple functional properties. Due to their compositionally complex nature, these HECs possessed better mechanical and high-temperature thermal

* Corresponding author.
** Corresponding author.
*** Corresponding author.
**** Corresponding author.
E-mail addresses: rajeshmishraphy@gmail.com, rajesh-kumar.mishra@bam.de (R.K. Mishra), f.minussi@unesp.br (F.B. Minussi), rohitrshahi@cusb.ac.in (R.R. Shahi), eudes.borges@unesp.br (E.B. Araújo).

https://doi.org/10.1016/j.ceramint.2025.09.256
Received 24 December 2024; Received in revised form 11 July 2025; Accepted 16 September 2025
Available online 17 September 2025

stability and other functional properties than conventional ceramics [6–8]. Yan et al. reported that $(MoTaTiVW)C_5$ HECs synthesized through the powder metallurgy route (ball milling + spark plasma sintering) displayed high hardness (19.63 GPa) and fracture toughness (6.25 MPa $m^{1/2}$) because of the combined toughening effects of SiC and multi-elemental particles [8].

From the first report on entropy-stabilized rock-salt structured high entropy oxide by Rost et al. in 2015 [9], various structured high entropy oxides (such as spinel, perovskite, pyrochlore, magneto-plumbite, etc.) have been reported since then [10–15]. In all, spinel (AB_2O_4) and perovskite (ABO_3) structured HEOs gained significant attention from researchers because of their versatility, numerous oxygen vacancies, and having two sub lattice sites (A- and B-sites), which make them potential candidates for tailored multifunctional properties [2–4,16]. Spinel oxides (having the general formula AB_2O_4) are an important group of materials with distinctive applications in catalysts, magnetic recording, electrical, sensors, microwave industry, etc. [15–22]. Due to their two sub-lattice tetrahedral (A) and octahedral (B) sites, the properties of spinel oxides can be tailored by introducing different cations at A- and/or B-sites. Introducing different chemical elements in spinel oxide at A- and/or B-sites changes the magnetic, electrochemical, and optical properties [15–22]. A literature review suggests spinel-structured HEOs have distinctive magnetic, catalytic, energy storage, and other functional properties compared to conventional spinel oxides [15–22]. Besides the magnetic, catalytic, and energy storage properties of high entropy spinel (HES), only a few studies have been reported on the electrical properties of spinel HEOs [23–26]. As ferrites have been widely studied as semiconducting materials and have potential applications in electric, dielectric, and microwave absorption properties, more studies are required to understand and explore spinel HEOs' compositional space and physicochemical structure-property correlation for harsh environment applications [23–26]. Zheng et al. studied the pressure dependence (up to ~ 20 GPa) structural and dielectric properties of spinel $(FeCoCrMnZn)_3O_4$ HEO [26]. They reported that with increased pressure, the electrical resistance of the HEO decreased exponentially, while dielectric permittivity decreased linearly. In addition, they also reported that the prepared spinel HEO displayed good frequency stability and dielectric characteristics at both low and high pressures, indicating its potential applications in harsh environmental conditions [26]. This suggests that the high-entropy spinel (HES) phase represents a new frontier in materials design, offering an extensive opportunity to tune a wide range of multifunctional properties by doping multiple cations at A- and/or B-sites.

Literature data suggest that the choice of synthesis method has a substantial impact on both the microstructure and resulting functional properties of ceramics [27–29]. Among the various techniques, the mechanochemistry solid-state reaction route is widely recognized for producing ceramics with superior homogeneity and finer grain sizes compared to other methods [27–29]. Unlike sol-gel techniques, which typically require organic precursors and involve complex drying and calcination steps, solid-state mechanochemistry avoids the use of solvents, reducing both processing time and environmental impact. Utilization of ball milling for a defined duration (typically 5–10 h) not only ensures better homogenization of powder particles but also enhances the diffusion kinetics of the constituent oxides in the mechanochemistry. This is achieved by reducing the activation energy, which is attributed to defect formation during the milling process [19,23,30]. Furthermore, ball milling for an appropriate duration results in a lower sintering temperature compared to the conventional solid-state reaction method [19,23,30]. When compared to alternative synthesis approaches such as sol-gel, hydrothermal, or sputtering, the mechanochemical solid-state method facilitates achieving near-nominal stoichiometric composition in the final ceramic product, and also offers a unique balance of simplicity, scalability, and material quality [29,31]. The literature indicates that the change in synthesis route affects the morphology of the $(Co,Cr,Fe,Ni,Mn)_3O_4$ spinel high-entropy oxides, drastically changing their functional properties [32–35].

The selection of doping elements and processing conditions also affects the microstructure and functional properties of high entropy materials [36–41]. Duan et al. synthesized a series of $(FeCoNiCrMnXLi)_3O_4$ (X = Cu, Mg, Zn) spinel HEO through the solid-state method to investigate the effect of the addition of cations on microstructure and energy storage behavior [36]. All three HEOs exhibit a single-phase spinel structure and better lithium storage performance. The Zn-doped $(FeCoNiCrMnZnLi)_3O_4$ spinel HEO yields higher specific capacitance than the Cu and Mg-doped spinels. The author reported that the better specific capacity of Zn-doped oxide is related to its small particle size and relatively larger lattice parameters than the other two spinel HEOs [36]. Despite the selection of doping elements, processing conditions (such as sintering/annealing temperature, sintering atmosphere) not only affect the structural and microstructural characteristics but also create defects in the lattice that extensively affect the resultant properties of the ceramics [39,40]. Kaushiga et al. studied the effect of sintering temperature on structural, resistive switching (RS), and dielectric properties of bulk $Ba_{0.7}Sr_{0.3}TiO_3$ oxide synthesized through solid-state method [39]. They used a modified double-step sintering (DS) and conventional single-step sintering (CSS) approach and sintered the samples at two different temperatures (1250 °C and 1350 °C). The grain size distribution was enhanced for DS-processed material compared to the CSS-processed sample. With the change in sintering temperature, the ceramic's dielectric and resistive switching behavior changed extensively. The high-temperature sintered ceramic displayed higher frequency-dependent behavior, whereas the 1250 °C sintered ceramic yielded lower frequency-dependent behavior. In addition, the RS behavior also changed with the sintering temperature. They reported that the enhanced RS behavior of ceramics has been associated with the redistribution of cations, oxygen vacancies, and ferroelectric domain orientation [30]. Moreover, Pithan et al. also found that the dielectric properties of the $Ba_{0.45}Mg_{0.05}Sr_{0.5-x}Ca_xTiO_3$ perovskite structured HECs changed drastically with the variation of sintering temperature [40].

Considering the beneficial effect of processing conditions, in the present study, we aimed to synthesize a single-phase spinel composition and investigate the effect of sintering temperature on the structural, microstructural, and dielectric properties of Co-Fe-Ni-Al-Ti-O-based HEOs. The compositional selection of the HEO is derived from the mostly studied $(CoFeNiMnCr)_3O_4$ [32], and other CoFeNi-based spinel ceramics [15,18,22,36]. In addition, the selection of sintering temperature (i.e., 1000, 1100, and 1250 °C) is also related to the literature data of HECs synthesized through the solid-state reaction method [15,19,23,24,32]. The selected composition of the HEO has been synthesized through the solid-state mechanochemistry method. The mechanochemistry route is an efficient, low-cost, faster reaction kinetics and eco-friendly synthesis route compared to other available synthesis routes [30]. Detailed microstructure and dielectric property-correlation of the synthesized Co-Fe-Ni-Al-Ti-O-based HEO has been explored with the help of fractal and impedance spectroscopy analyses. Surface morphology plays an important role in governing the functional properties of the ceramics [42,43]. Fractal analysis, which is a scale and resolution invariant technique, provides deeper information about the complexity and irregularity (such as intergranular contacts/grain boundary geometry, etc.) of the surface morphology by calculating the fractal dimension. Literature review implies that the fractal dimension (D_f) of a surface can be computed through various techniques such as the power spectral density (PSD) method, de-trended fluctuation analysis (DFA), cubic counting, etc. [42–44]. Among all these methods, the Higuchi algorithm approach provides prompt and precise calculation with maximum accuracy for the fractal dimension calculation. Literature reviews showed that the Higuchi algorithm has been employed in various fields of science to get better insights into surface morphology and property correlation [42–44]. Using the fractal dimension value, one can also calculate the Hurst exponent, which gives the surface roughness/irregularities on a small scale. The values of the Hurst

exponent vary between 0 and 1, and it has been found that the lower value of the Hurst exponent gives high complexity at a small scale [42,43]. A detailed description of the Higuchi algorithm and fractal theory can be found in various references [42–44]. Despite the fractal analysis, complex impedance spectroscopic analysis is also a prominent technique in solid-state physics to understand the conduction mechanism of the synthesized ceramics in a wide range of frequency-dependent dielectric behavior and relaxation characteristics. The impedance analysis can provide the electrical conduction contribution of the grain, grain boundary, and materials-electrode separately [45,46].

2. Materials and methods

The polycrystalline $(Co_{0.2}Fe_{0.2}Ni_{0.2}Al_{0.2}Ti_{0.2})_3O_4$ multi-cations spinel oxide was synthesized using solid-state mechanochemistry. The precursors Co_3O_4 (99.9 %), Fe_2O_3 (99.5 %), TiO_2 (99.0 %), Al_2O_3 (99.0 %), and NiO (99.5 %) powders in equimolar proportions were mixed and ball milled (through a planetary ball miller) for 5 h (hr) under wet milling conditions using zirconia balls as grinding media. The ball-to-powder ratio (BPR) was 25:1, and Toluene was used as a process control agent (wet milling media) to prevent agglomeration during milling and to homogenize the powder particles. Literature data suggest that the use of Toluene as a wet milling medium, compared to others (such as ethanol and acetone), favors the production of fine powder particles with better homogeneity [47,48]. These homogeneous fine-particle powders will benefit the sintering process by enhancing the diffusion kinetics. The characteristic features (melting temperature, molar mass, ionic radius, etc.) of the precursors are given in Table S1. After ball milling, the powder mixture was extracted from the vial and dried for 24 h period at 60 °C in an electric oven. The dried powder was pelletized using a mold with a pressure of 10 tons through a hydraulic press machine with a holding time of 5 min. The obtained pellet was sintered for the final chemical reaction at three different 1000 °C, 1100 °C and 1250 °C temperatures for 10 h, followed by air quenching (AQ). The obtained final product was further characterized through X-ray diffractometry (XRD, Rigaku Ultima IV) for phase formation analysis using Cu-K_α radiation ($\lambda = 1.5405$ Å) in the 2θ range of 10° to 100° with 0.02° step size and continuous scan with scan rate 2°/min. The XRD patterns obtained were fitted through the Le Bail refinement using JANA-2006 software for crystallographic analysis. The room temperature Raman spectra were recorded through the Raman spectroscopy (BX51-Voyage™) in the frequency range of 100–1000 cm^{-1} with a laser excitation source having a wavelength of 785 nm. Field emission scanning electron microscopy (FE-SEM, Carl Zeiss EVO LS15) examined the sample's morphology. The elemental mapping of the sample was further analyzed through the energy dispersive X-ray spectroscopy (EDS, Bruker) equipped with the FE-SEM (Gemini, LEO 1530 VP). For dielectric measurement, the gold electrode was deposited using a shadow mask on the top surface of the pellet through sputtering. The gold electrode was also deposited over the entire region of the bottom surface of the pellet using sputtering. The frequency-dependent electrical behavior was studied at room temperature through data acquired using an Agilent 4284A LCR meter in the frequency range of 500 Hz to 1 MHz with an applied electric bias voltage of 300 mV. The recorded conductance (G) and susceptance (B) data from the LCR meter were utilized to determine the ac conductivity ($\sigma = GL/A$), complex dielectric permittivity ($\varepsilon^* = \varepsilon' - i\varepsilon''$), and complex impedance ($Z^* = Z' - iZ''$), where L is the distance between electrodes (i.e., the sample thickness), and A the electrode area. The fractal analysis was performed by using the Higuchi algorithm on SEM micrographs. The obtained SEM micrographs were processed through WSxM 5.0 software to obtain discretized height data. The height data was then analyzed using the Higuchi algorithm through MountainLab®Premium 9.3 software.

3. Results and discussion

3.1. Structural (XRD and Raman) analysis

Fig. 1 shows the XRD patterns of hand-mixed, ball-milled, and different temperature sintered Co-Fe-Ni-Al-Ti-O mixture. XRD pattern of hand-mixed sample reflects diffraction reflections of all constituent oxide precursors. After 5 h ball milling, the peak width (FWHM) increases, which indicates the insertion of defects during ball milling in the precursor crystallites. Introducing defects enhances the diffusion kinetics by decreasing the precursors' activation energy and enhancing the solid solution phase formation probability during sintering [19,21,23,49]. After sintering at 1000 °C, the XRD pattern shows the new phase formation along with constituent oxide precursors. The presence of oxide precursors after 1000 °C sintering temperature indicates that 1000 °C is not sufficient to diffuse the constituent oxides to form a new solid solution phase. Enhancing the sintering temperature from 1000 °C to 1100 °C, the XRD pattern shows that all constituent oxides peaks disappeared and a single cubic spinel phase (having space group $Fd\bar{3}m$) formed. Besides, to check whether the sample also forms a single spinel phase at high temperature or not, we further sintered the mixture (ball milled) of the sample at 1250 °C following the same sintering conditions. The XRD pattern of the 1250 °C sintered sample also displayed that all constituent oxide peaks disappeared and a single cubic spinel structure formed, similar to the 1100 °C sintered sample. The phase formation analysis was performed through the JANA-2006 software using Le-Bail refinement (Fig. S1). From the XRD patterns, it can also be seen that with the enhancement of sintering temperature (from 1100 to 1250 °C), the peak position shifted towards a lower 2θ angle, and crystallinity was enhanced. The peak shift towards the lower angle indicates that the lattice parameter increases, which might be associated with the change in cations distribution order at the tetrahedral (A) and/or octahedral (B) site [50,51]. By refinement, the found lattice parameters of the sintered spinel HEOs are close to the $NiFe_2O_4$ inverse spinel oxides (JCPDS No. 5910064) [45,51–54]. The lattice parameters and unit cell volume of the formed spinel phases for 1100 °C and 1250 °C sintered ceramics are found to be 8.3245(4) Å, V = 576.9 $Å^3$ and 8.3368(3) Å, V = 579.4 $Å^3$ respectively. The crystallite size and lattice strain corresponding to the most intense peak (113) of the formed spinel phase of the different temperature sintered ceramics have also been computed through the Pseudo-Voigt functional analysis [42,55]. It has been found that with the increase of sintering temperature from 1100 °C to 1250 °C, the crystallite size enhances from 36.18 ± 0.01 nm to 46.36 ± 0.01 nm, and lattice strain decreases from 0.32 ± 0.02 % to 0.25 ± 0.02 %. Despite crystallographic parameters, the hopping length and other spinel ferrite structural parameters have also been determined using the following relations [56,57]. The calculated structural parameter results are given in Table 1.

$$\text{Octahedral hopping length} : L_B = \frac{a}{4}\sqrt{2} \tag{1}$$

$$\text{Tetrahedral hopping length} : L_A = \frac{a}{4}\sqrt{3} \tag{2}$$

$$\text{Octahedral bond length} : d_{Bx} = a\sqrt{3u^2 + \left(\frac{43}{64}\right) - \left(\frac{11}{4}\right)\text{u}} \tag{3}$$

$$\text{Tetrahedral bond length} : d_{Ax} = \left(u - \frac{1}{4}\right)a\sqrt{3} \tag{4}$$

$$\text{Shared octahedral edge} : d_{BxE} = \sqrt{2}(1 - 2u)a \tag{5}$$

$$\text{Tetrahedral edge} : d_{AxE} = \sqrt{2}\left(2u - \frac{1}{2}\right)a \tag{6}$$

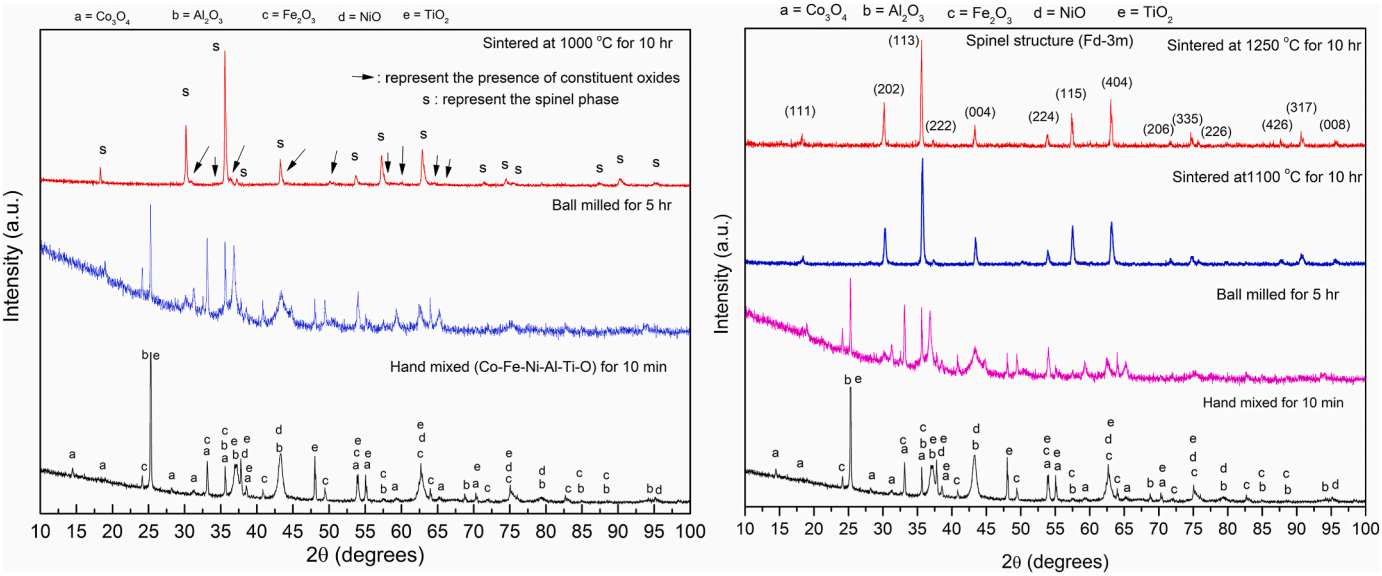

Fig. 1. X-ray diffraction patterns of hand-mixed, ball-milled, and Co-Fe-Ni-Al-Ti-O mixture sintered at 1000 °C, 1100 °C, and 1250 °C for 10 h.

Table 1
Spinel structural parameters (hopping length, bond length, etc.) of HEOs.

Composition	Processing Condition	a (Å)	L_A (Å)	L_B (Å)	d_{Bx}(Å)	d_{Ax} (Å)	D_{BxE}(Å)	d_{AxE} (Å)	D_{BxEU} (Å)
$(Co_{0.2}Fe_{0.2}Ni_{0.2}Al_{0.2}Ti_{0.2})_3O_4$	Sintered at 1100 °C, AQ	8.3245	3.6045	2.9427	0.2601	1.8022	2.9427	2.9427	0.5202
	Sintered at 1250 °C, AQ	8.3368	3.6098	2.9470	0.2605	1.8049	2.9470	2.9470	0.5210

$$\text{Unshared octahedral edge}: d_{BxEU} = \sqrt{4u^2 + \frac{11}{16} - 3u} \quad (7)$$

Here, a is the lattice parameter of the cubic spinel phase, and u is the oxygen positional parameter. The oxygen positional parameter can be determined by using $u = \left[(r_A + r_O)/a\sqrt{3} + 1/4\right]$ [56,57]. Here, r_O is the radius of the oxygen ion and r_A is the mean ionic radius of the tetrahedral A-site. Due to the unavailability of the oxygen positional parameter for the present spinel HEO composition, we used $u = 0.375$ (for ideal FCC) for simplicity [56,57]. From Table 1, with the change of sintering temperature, the hopping length, bond length, and other spinel structural parameters at the A- and B-site displayed interesting temperature-dependent characteristics. Because their temperature response involves thermal expansion and exchange of cation orders at the A and/or B-site. This change in hopping length, bond length, and other spinel structural parameters at B and/or A-site will inevitably affect the electrical properties of the spinel ceramics.

Beyond the structural characterization through XRD, Raman spectroscopic characterization was also performed to analyze both 1100 °C and 1250 °C sintered spinel HEOs (Fig. 2). As mentioned in the XRD analysis, the crystal structure of the synthesized $(Co_{0.2}Fe_{0.2}Ni_{0.2}Al_{0.2}Ti_{0.2})_3O_4$ is cubic with $Fd\bar{3}m$ space group symmetry. Literature data shows that for $Fd\bar{3}m$ space group symmetry, group theory predicts five active Raman phonon modes: A_{1g}, E_g, $3T_{2g}$ at an ambient condition [45,46,50]. From Fig. 2, these five active Raman phonon modes are visible with good intensity in the Raman spectra of HEOs sintered at different temperatures (1100 °C and 1250 °C). The observed phonon modes match well with the Co_3O_4 [58], $NiFe_2O_4$ [45,50,59], and Fe_3O_4 [60] spinels. A close analysis of these obtained spectra for both ceramics indicates that each peak reflects an asymmetric nature (i.e., doublet). The asymmetric nature of the Raman peaks indicates that the synthesized HEOs have mixed or inverse spinel structures. The obtained Raman spectra's asymmetric nature is associated with the distortion in metal-oxygen (M − O) bond distances [45,59]. Due to the multi-cations' substitution at A- and B-sites with ions of different ionic radii (Table S1), the M − O bond distances in the HEOs distort extensively, which lowers the symmetry, and the Raman spectra detect these changes substantially [45,59]. Moreover, it has been pointed out that the strongest phonon mode above 600 cm^{-1} belongs to the oxygen atom motion in the AO_4 group (i.e., tetrahedral group), and the phonon mode below 600 cm^{-1} is associated with the oxygen atom motion (bending/stretching) at the octahedral BO_6 group [45,46,59]. Therefore, the highest phonon mode above 600 cm^{-1} (i.e., 751 cm^{-1}) in the spinel $(Co_{0.2}Fe_{0.2}Ni_{0.2}Al_{0.2}Ti_{0.2})_3O_4$ HEO belongs to the A_{1g} symmetry. The phonon mode at about 408 cm^{-1} is associated with the E_g symmetry, which is related to the symmetric bending of oxygen atoms concerning cations in tetrahedral surroundings. The assigned $T_{2g}(2)$ and $T_{2g}(3)$ symmetry in Fig. 2 is associated with the vibration of the octahedral (BO_6) group. The asymmetric stretching causes $T_{2g}(2)$ symmetry, and $T_{2g}(3)$ is caused by the asymmetric bending of oxygen in the octahedral (BO_6) group. The assigned $T_{2g}(1)$ symmetry at about 185 and 255 cm^{-1} in Fig. 2 is related to the translational vibrations of the tetrahedron.

3.2. Sintering mechanism and microstructural analysis

Sintering is a thermal process that transforms particulate materials into dense solids through diffusion-driven densification and coarsening. The main driving force for sintering is the reduction of the total interfacial energy, which can be expressed as $\Delta(\gamma A) = \Delta\gamma A + \gamma\Delta A$. Here, γA is the total interfacial energy, where A is the total surface (interface) of the compact and γ is the specific surface (interface) energy. In the equation, the change in interfacial energy ($\Delta\gamma$) is associated with densification, and the change in interfacial area (ΔA) is related to the grain coarsening [61]. It has been reported that due to their higher surface area, fine particles sinter more rapidly than larger ones. Besides, the sintering mechanism is generally governed by dissolution-based mass transport, which involves a sequence of dissolution, mass transfer, and precipitation steps. This process is thermally activated and relies on atomic diffusion, which occurs through two primary transport mechanisms: **surface transport** and **bulk transport** [61]. When sintering occurs

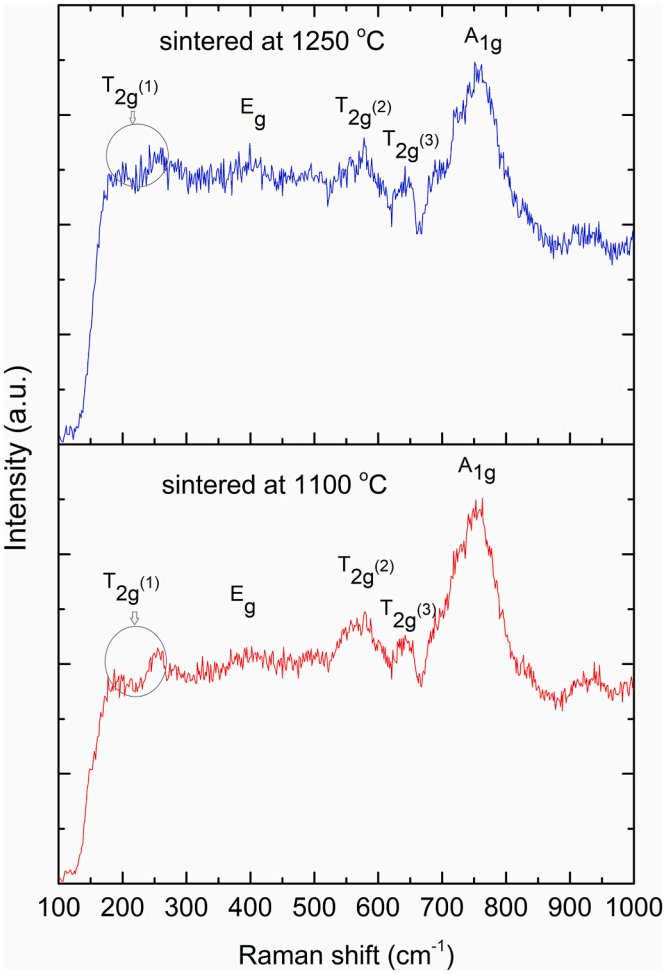

Fig. 2. Raman spectra of spinel HEOs sintered at 1100 °C and 1250 °C.

between two particles, a neck forms at the point of contact. In surface transport, material moves along the surface without contributing to overall shrinkage or densification. Key contributors to this mechanism are *surface diffusion* and *evaporation-condensation*, with surface diffusion playing a dominant role during the low-temperature sintering of metals and ceramics. However, bulk transport leads to shrinkage and densification, as material moves from the particle interior to the neck. Bulk transport involves mechanisms such as **volume diffusion, grain boundary diffusion, plastic flow, viscous grain flow,** lattice diffusion, and typically occurs at higher temperatures. While both transport modes contribute to neck growth, only bulk transport results in significant densification of the structure [62,63].

The sintering variables (materials and thermodynamics) also influence the microstructure, densification, grain growth, and diffusion processes during the sintering of materials [61]. The materials variable comprises the powder's chemical composition, the powder particles' shape and size, and the particle size distribution. Meanwhile, thermodynamic variables include temperature, sintering time, atmosphere, heating and cooling rates, etc [61]. In the present study, the material variables are constant for all sintered samples, as the precursor powders were ball milled for 5 h to enhance homogeneity before the sintering process. In addition, all the thermodynamic variables have also remained the same for the sintered samples, except for the temperature variable; therefore, the change in the microstructure, grain growth, and diffusion process in our study is only associated with the temperature effect.

The effects of the temperature variable and sintering kinetics can be observed in the microstructure and grain growth. Fig. 3(a), (b), and 3(c) summarize the FE-SEM images of the high entropy $(Co_{0.2}Fe_{0.2}Ni_{0.2}Al_{0.2}Ti_{0.2})_3O_4$ spinel oxide samples sintered at 1000 °C, 1100 °C, and 1250 °C for 10 h, respectively, at two different (10.00 KX and 30.00 KX) magnifications. The effect of the temperature variable on the microstructure and grain growth is clearly shown in Fig. 3. At lower temperatures, limited atomic mobility results in the initial formation of necks between particles, primarily driven by surface diffusion, as observed in Fig. 3(a) for the sample sintered at 1000 °C. As the temperature rises, lattice and grain boundary diffusion dominate, facilitating densification and the coalescence of grains, as observed in Fig. 3 (b) and (c) for the samples sintered at 1100 °C and 1250 °C, respectively. This kinetic is accompanied by significant grain growth, particularly near the final-stage sintering regime [61–63].

The sintering mechanism evolves significantly with the three studied temperatures. At the sintered sample at 1000 °C, the limited thermal energy leads to incomplete solid-state diffusion, resulting in a multiphase composition, as evidenced by XRD and SEM, in Figs. 1 and 3(a). The presence of residual constituent oxides indicates that grain boundary mobility and densification were insufficient, suppressing the grain growth. At 1100 °C and 1250 °C, the enhanced atomic diffusion promotes complete reaction among the precursors, facilitating the formation of a single-phase cubic spinel structure. By increasing the temperature to 1250 °C, grain growth becomes more pronounced due to active lattice diffusion, which reduces porosity and improves microstructural homogeneity, as shown in Fig. 3(c). These microstructural changes will undoubtedly affect the dielectric performance of the different temperature-sintered samples. However, excessive grain growth at 1250 °C may also introduce local variations in grain boundary density, possibly moderating the dielectric gains beyond a certain threshold. In Fig. 3(c) and (d), a polygonal morphology is observed in aggregates with different particle sizes, such that the increase in sintering temperature from 1100 °C to 1250 °C results in an increase in aggregated particle size and a decrease in porosity. The aggregated average particle sizes for the 1100 °C and 1250 °C sintered samples were 0.76 μm and 1.82 μm, respectively, as calculated from the 5 K magnification SEM micrograph in Fig. S2. The analysis reveals a more uniform and homogeneous distribution of aggregated particle size for the sample sintered at 1250 °C than 1100 °C. Fig. S2(d) confirms the uniformity of the homogeneous particle distribution for this sample. In addition, elemental analyses in the representative sample sintered at 1100 °C, as shown in Fig. S3, indicate that each aggregated particle contains all the composing elements and confirms the equimolar nominal composition for this sample.

3.3. Fractal analysis

Surface morphology plays a crucial role in determining the functional properties of ceramics and thin films, such as electrical, magnetic, electrochemical, etc. [42–44,64,65]. Advanced high-resolution spectroscopy and microscopy techniques, such as SEM AFM, TEM, etc., enable the detailed examination of surfaces' crystallographic, electronic, and chemical properties and interfaces on an atomic scale. These studies highlight the critical influence of defects, additives, or impurities on the characteristics of these materials. Furthermore, fractal theory offers an intriguing mathematical framework to address specific challenges, including wetting phenomena, sol-gel synthesis, or ceramic sintering [65]. Fractal analysis, characterized by its independence from scale and resolution, enhances our understanding of surface morphology by determining the fractal dimension, which reveals the complexity and irregularity (such as intergranular contacts/grain boundary geometry, etc.) of the structures. Moreover, it also helps to understand the microstructure and functional property correlations [42–44]. Apart from the fractal behavior of thin films [42–44], Mitic et al. [64] reported that ceramic materials also possessed a fractal configuration nature. In the context of ceramic surfaces, this encompasses not only the outermost layer but also features like porosity, intergranular contacts, and the

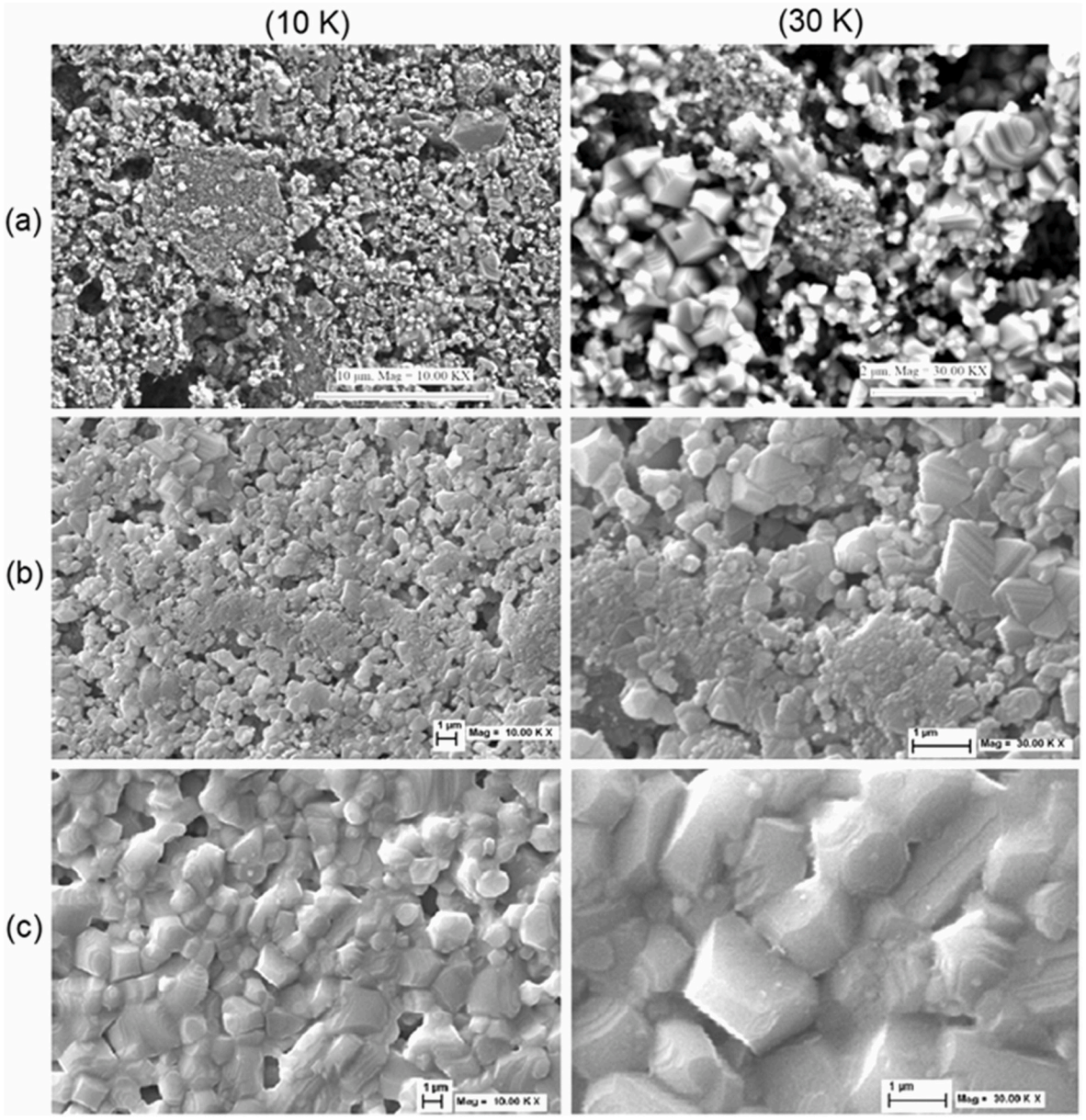

Fig. 3. FE-SEM micrographs of the $(Co_{0.2}Fe_{0.2}Ni_{0.2}Al_{0.2}Ti_{0.2})_3O_4$ spinel high entropy oxide samples sintered at (a) 1000 °C, (b) 1100 °C, and (c) 1250 °C for 10 h. Images are shown at the 10 K and 30 K magnifications.

geometry of grain boundaries. They pointed out that the emergence of fractality in ceramics is associated with the shape of the ceramic grains/particles, negative space in the ceramics, and Brownian motion within the ceramics. They explained that the ceramic grains/particles are a fractal surface viewed as a contour on a surface. Since the powder particles are porous, during the ceramic processing and sintering, the negative space is available within the ceramics. These negative spaces are associated with the porosity and intergranular spaces in the ceramics. In addition, the Brownian motion within the ceramic is related to the micro-particle flow of ions, electrons, and atoms during and after the sintering of materials [64].

Both bulk and surface characteristics influence dielectric properties in ceramics, but the extent of influence depends on the specific material and its application. Bulk characteristics, such as grain size, density, and phase composition, often significantly determine the overall dielectric constant and loss. These properties are influenced by factors like sintering temperature and material composition [66,67]. Surface characteristics, on the other hand, can also affect dielectric behavior. For example, surface defects, roughness, intergranular contacts, geometry of grain boundaries, and contamination can affect the dielectric response of the material [68,69]. Thus, to analyze the complexity of the surface of the different temperature-sintered spinel HEOs, the SEM micrograph of both HEOs was quantitatively examined using fractal theory. The fractal analysis (fractal dimension) of the synthesized spinel HEOs has been analyzed using the Higuchi algorithm, which is an important approach to determining the fractal dimension (D_f) directly [42–44]. The discretized height data derived from the SEM micrographs (Fig. S2(a and c)) have been utilized for evaluating the D_f of the horizontal section of the surface. A detailed description of the Higuchi algorithm can be found elsewhere [42–44]. In brief, the Higuchi algorithm is defined here. The Higuchi algorithm is an effective and direct method for evaluating the D_f from observed data for time series and many other domains. The height profile at each pixel of the surface along the horizontal section is designated by $R(1)$, $R(2)$, $R(3)$, …, $R(N)$. The k subsequences of the data can be constructed through the Higuchi method as follows:

$$R_n^k : R(n), R(n+k), R(n+2k), R(n+3k), \ldots\ldots\ldots\ldots, R(n+pk) \tag{8}$$

Here $n = 1, 2, 3, 4, \ldots., k$, and $p = int\left(\frac{(N-n)}{k}\right)$. The length $L_n(k)$ of each segment R_n^k is then represented as:

$$L_n(k) = \frac{\left[\left(\sum_{i=1}^{p} |R(n+ik) - R(n+(i-1)*k)|\right) * \frac{N-1}{pk}\right]}{k} \tag{9}$$

Here, N is the entire set of the data points, and $\frac{N-1}{pk}$ is the normalization constant. The average value of the length can be expressed as:

$$L(k) = \frac{\sum_{n=1}^{k} L_n(k)}{k} \tag{10}$$

According to power law, the length scale $L(k)$ with k resolutions can be expressed as:

$$L(k) \sim k^{-D_f} \tag{11}$$

Here, D_f is the fractal dimension and can be estimated from the gradient of $\log L(k)$ vs $\log k$ plot.

Fig. 4(a) and (d) shows the variation of $L(k)$ as a function of k at a double logarithmic scale, and the slope of the curve (i.e., $\log L(k)$ vs $\log k$) gives the fractal dimension of the high entropy ceramic surface. The solid red lines in Fig. 4(a) and (d) are the least squares fit to the data of the ceramic surface. The fractal dimension of the different temperature sintered spinel HEOs is 1.61 ± 0.05 (1100 °C sintered) and 1.53 ± 0.05 (1250 °C sintered). The results indicate that the fractality (i.e. complexity and irregularity) decreases with the increase of the sintering temperature. It has been reported that the higher fractality indicates a more irregular surface, while lower fractality depicts a smoother surface of the ceramic/thin films [42–44,64]. Therefore, the 1100 °C sintered ceramic has more crest (up) and trough (down) than the 1250 °C sintered spinel HEO. Barcelay et al. has also reported similar behavior for $EuMnO_3$ thin films with the enhancement of sintering temperature [70]. The fractality variation of both HEOs concerning the sintering temperature can also be seen graphically in Fig. 4(b) and (e), which shows the variation of D_f with the pixels.

Despite the fractal dimension, the Hurst exponent (H), which shows the complexity of the surface of ceramic/thin films at a small scale, has also been evaluated using the relation $H = 2 - D_f$ [42–44]. The value of the Hurst exponent varies between 0 and 1, and the lower value of H gives higher complexity at a small scale [42–44]. It has been reported that the value of $H = 0.5$ indicates Brownian motion or random walk. This means there is no correlation between the current and future observation data. In simple words, we can say that the points are independent, and there is no correlation between the height fluctuations at any pixels and neighboring pixels on a small scale. In addition, if the value of $H < 0.5$, then it indicates an antipersistent behavior, which means that a decrease/increase at any time step will most likely follow an increase/decrease. In other words, the height variations at neighboring pixels are negatively correlated. However, if the value of $H > 0.5$, then it indicates a persistent behavior. In this case, an increase/decrease in the observation data will most likely be followed by an increase/decrease in the short term at the successive time steps. This means that in a persistent behavior, the data shows the memory effect, and there is a positive correlation between the ceramic's surface heights at neighboring pixels [42–44,70]. Fig. 4(c) and (f) shows the variation of H with respect to the no. of row pixels for different temperature-sintered spinel HEOs. The Hurst exponent for the different temperature sintered spinel ceramic surfaces is 0.39 ± 0.05 (for 1100 °C sintered) and 0.47 ± 0.05 (for 1250 °C sintered). The found H values are less than 0.5, which indicates anti-persistent behavior. This means that an increase/decrease in height fluctuation at a small scale is likely a decrease/increase at a successive time step. In other words, the height variations at neighboring pixels are negatively correlated for both spinel HEOs at small scales.

3.4. Dielectric characteristics and ac conductivity

Fig. 5 shows the dielectric permittivity as a function of the frequency of spinel $(Co_{0.2}Fe_{0.2}Ni_{0.2}Al_{0.2}Ti_{0.2})_3O_4$ HEOs sintered at different temperatures. Fig. 5(a) shows that both HEOs displayed higher dielectric permittivity (ε') as compared to the conventional $NiFe_2O_4$ ferrites [59] and other conventional ceramics [71–73]. The higher dielectric permittivity of the synthesized spinel HEOs may be associated with substituting multi-cations at A- and/or B-sites. For HECs, severe lattice distortion and higher oxygen vacancies are present due to multi-cations

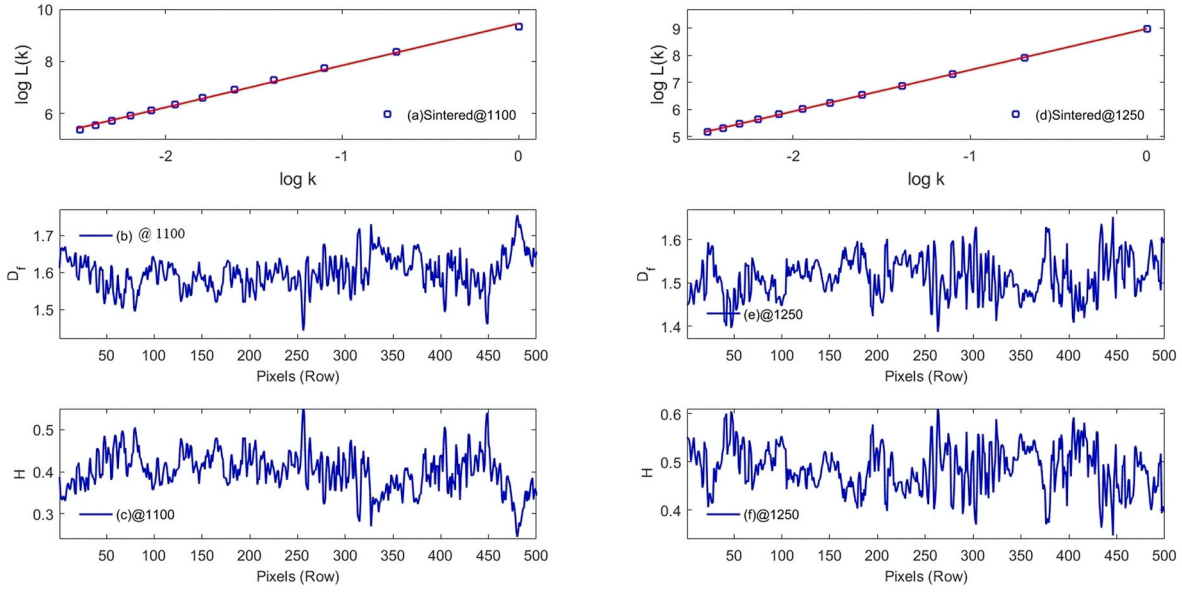

Fig. 4. Variation of (a,d) $\log L(k)$ vs $\log k$, (b,e) Fractal dimension (D_f) vs. pixels, and (c,f) Hurst exponent (H) vs. pixels for different temperature sintered spinel HEOs. Here, the red line (in Fig. (a) and (d)) corresponds to the plot that best fits the respective curve. (For interpretation of the references to colour in this figure legend, the reader is referred to the Web version of this article.)

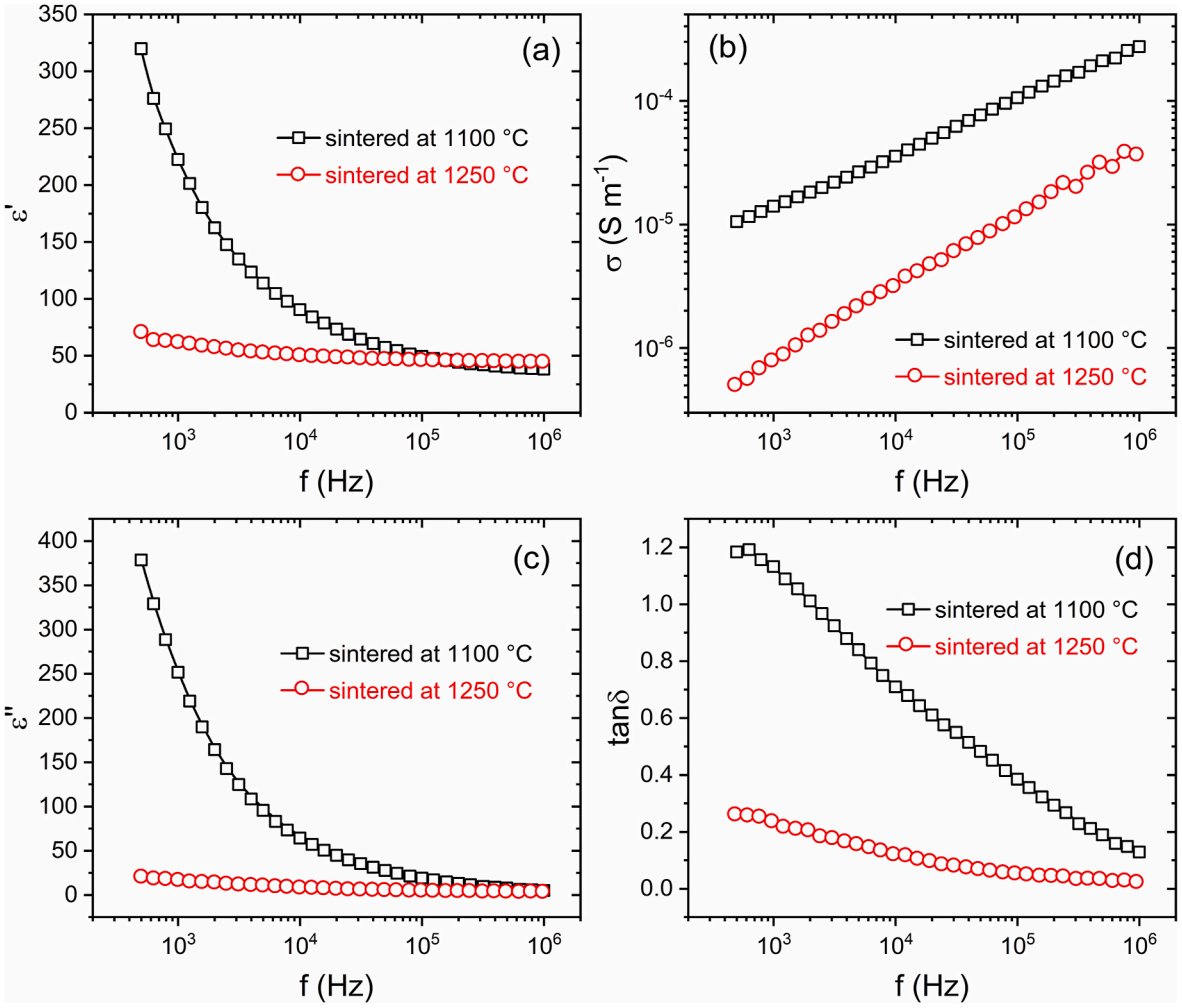

Fig. 5. Frequency-dependent dielectric permittivity ε' (a), ac conductivity σ (b), dielectric loss ε'' (c), and loss tangent tan δ (d) of different temperature sintered spinel HEOs.

(of different ionic radii) at A- and B-sites. The lattice distortion effect can be viewed from the Raman spectra analysis, which shows asymmetric (i.e., having doublet/shoulder peak) phonon modes. The formation of a defect cluster generates an electron pinning defect dipole effect that may contribute to polarization and increase the dielectric permittivity of the synthesized spinel HEO [74,75]. Moreover, both 1100 °C and 1250 °C sintered HEOs displayed frequency dispersion behavior. The observed decrease in dielectric permittivity with increasing frequency in HEOs is typical behavior of most dielectrics, often associated with the Maxwell–Wagner type of polarization effects [46,59,71,72].

At room temperature, the dielectric permittivity in cubic ferrites is the sum of interfacial (or space-charge), electronic, and ionic polarization [46,59,71,72]. The decrease in dielectric permittivity with increasing frequency can be explained by the Maxwell–Wagner polarization and Koop's phenomenological theory [46,59,76,77]. According to this, at low-frequency regions, the decrease in permittivity is attributed to the loss of interfacial or space charge polarization and ε' tends to a constant value at high frequencies, related to the sum of electronic and ionic contributions [46,59,76,77]. From Fig. 5(a), it can be seen that the 1100 °C sintered HEO displayed high permittivity at low and moderate frequencies as compared to the 1250 °C sintered spinel HEO (Table 2). In addition, the 1100 °C sintered ceramic also shows relatively higher frequency-dependent dielectric behavior than the 1250 °C sintered ceramic. Literature data imply that the dielectric permittivity of the materials is highly sensitive to the doping elements, crystallinity, interfacial polarization effect, grain size, and defect formation [46,59,76–78]. From the fractal analysis on SEM micrograph, we found that with the increase in sintering temperature, the fractality (i.e., D_f) decreases, whereas the average aggregated particle/grain size increases. In a sense, the surface complexity is a reflex of the regular and uniform distribution of grains and particle aggregates. With larger grains and aggregates, the tendency is to lower surface complexity, as observed. Since the dielectric characteristics are very sensitive to the surface and microstructural morphology [79–81], the decrease in permittivity for 1250 °C sintered ceramic is associated with the decrease in complexity of surface morphology, or, in other words, the increased change in

Table 2
Dielectric properties of $(Co_{0.2}Fe_{0.2}Ni_{0.2}Al_{0.2}Ti_{0.2})_3O_4$ spinel High Entropy Oxide.

Composition	Processing Condition	Dielectric permittivity (ε')			Loss tangent (tanδ)		
		1 kHz	10 kHz	1 MHz	1 kHz	10 kHz	1 MHz
$(Co_{0.2}Fe_{0.2}Ni_{0.2}Al_{0.2}Ti_{0.2})_3O_4$	Sintered at 1100 °C, AQ	223	91	39	1.13	0.71	0.13
	Sintered at 1250 °C, AQ	61	50	44	0.22	0.11	0.01

particle/grain size. As space charge polarization is highly dependent on the existence of interfaces/surfaces/grain boundaries, increased grain sizes reduce the interface/grain boundary area, diminishing ε'. Moreover, the relatively less frequency-dependent dielectric behavior of 1250 °C sintered ceramic is associated with having a more uniform distribution of particles/grains than the 1100 °C sintered ceramic [39]. The uniform distribution of grains/particles generates less internal stress, which results in easier dielectric polarization [78].

The ac electrical conductivity (σ) of both 1100 °C and 1250 °C sintered spinel HEOs has also been evaluated and shown in Fig. 5(b). From the figure, it can be seen that for both HEOs, the ac conductivity increases steeply with the increase of frequency. Literature data imply that the frequency-dependent conductivity of the ceramics generally obey Jonscher's power law defined as $\sigma(\omega) = \sigma_{dc} + B\omega^n$ $(0 < n < 1)$ [46,82]. Here, σ_{dc} is the frequency-independent conductivity, ω is the angular frequency, and B and n are empirical parameters. A general explanation for the observed dispersion is that, at lower frequencies, the charge carriers travel longer distances and have an enhanced probability of being scattered during transport. That means that, in general, carriers face reduced mobility, which means lower conductivity. With increasing frequencies, carriers travel progressively lower distances and have a lower probability of being scattered during transport. In other words, the average mobility and observed conductivities are higher.

Another important experimental observation is that the sample sintered at 1100 °C displayed much higher conductivity than that at 1250 °C. A detailed discussion of the possible causes of that is given in the next section. Now, we focus on the consequences of the energy losses resulting from the conductivities. The properties directly related to these energy losses are the dielectric loss (ε'') and the loss tangent ($\tan\delta = \varepsilon''/\varepsilon'$), shown respectively in Fig. 5(c) and (d). The frequency-dependent behavior of ε'' in Fig. 5(c) can be explained on a similar basis to the conductivity behavior. At low frequencies, charge carriers have time to be conducted through long distances, which increases the losses through Joule effects. In contrast, charge carriers have enough time to be transported for long distances at high frequencies, and the energy losses through Joule effect will be lower. Since ε'' and $\tan\delta$ are directly related, the behavior in Fig. 5(d) is essentially the same as observed in Fig. 5(c). Noteworthy, as expected from the conductivity values, both ε'' and $\tan\delta$ are lower for the sample sintered at 1250 °C than 1100 °C throughout the entire frequency range. In particular, the found $\tan\delta$ value 0.01 (at 1 MHz) for 1250 °C sintered HEO is very low compared to the 1100 °C sintered HEO and many other conventional ceramics [73]. Thus, the synthesized 1250 °C sintered spinel HEO having low dielectric loss could be exploited at higher frequency applications. The dielectric permittivity (ε') and loss tangent ($\tan\delta$) values of both sintered samples at 1100 °C and 1250 °C have also been compared with conventional oxides and some HEO (Table 3) [59,83–100]. From Tables 3 and it can be seen that the synthesized HEOs possessed better dielectric properties at 1 kHz and 1 MHz frequencies as compared to the conventional oxides.

3.5. Impedance spectroscopy data analysis

Complex impedance spectroscopy is an effective tool in solid-state physics to analyze the conduction mechanism of synthesized thin-films and ceramics. Despite magnetite being a textbook, widely acknowledged electronic semiconductor [101], typical values observed at room

Table 3
Comparison of Dielectric properties with conventional spinel oxides and some HEOs.

Composition	Dielectric Permittivity (ε')		Loss Tangent (tan δ)		Ref.
	at1 kHz	at 1 MHz	at 1 kHz	at 1 MHz	
$NiFe_2O_4$	60.06	32.20	0.62	0.03	[59]
$Cu_{0.5}Ni_{0.5}Fe_2O_4$	~600	–	~60	–	[83]
$Li_{0.2}Zn_{0.6}Fe_{2.2}O_4$	112	–	0.23	–	[84]
$CdFe_2O_4$	~113	–	~0.90	–	[85]
$Li_{0.2}Cd_{0.6}Fe_{2.2}O_4$	~32	–	~0.36	–	[85]
$Li_{0.3}Cd_{0.4}Fe_{2.3}O_4$	~18.21	–	~0.13	–	[85]
$Co_{0.32}Zn_{0.68}Fe_2O_4$	~5	–	~0.2	–	[86]
$Co_{0.49}Zn_{0.51}Fe_2O_4$	~9	–	~0.8	–	[86]
$Co_{0.79}Zn_{0.21}Fe_2O_4$	~9	–	~03	–	[86]
$Mg_{0.25}Zn_{0.75}Fe_2O_4$	~17	–	~0.4	–	[86]
$MnFe_2O_4$	$\sim 5 \times 10^5$	–	~0.99	–	[87]
$CoFe_2O_4$	~1000	–	–	–	[88]
$CuFe_2O_4$	~280	~320	~0.2	~0.05	[89]
$NiFe_2O_4$	~230	~240	~0.1	~0.05	[89]
$Ni_{0.6}Cu_{.4}Fe_2O_4$	~230	~240	~0.1	~0.05	[89]
$Co_{0\text{-}8}Ni_{0\text{-}2}Cr_2O_4$	~10	~4	~0.1	~0.05	[90]
$CoFe_2O_4$	–	~28	–	–	[91]
$SrFe_2O_4$	–	~6	–	–	[91]
$Co_{0.6}Sr_{0.4}Fe_2O_4$	–	~13	–	–	[91]
$Cu_{0.7}Zn_{0.3}Fe_2O_4$	~40	~25	~0.2	~0.1	[92]
$MgFe_2O_4$	~31	–	~0.9	–	[93]
$Mg_{1\text{-}x}Zn_xFe_2O_4$ (x = 0.2,0.4,0.6,0.8)	~3 - 1200	–	~0.13–4.4	–	[93]
$ZnFe_2O_4$	3.0×10^5	–	0.7	–	[93]
$Ni_{0.4}Cu_{0.2}Zn_{0.4}Fe_2O_4$	~15	~11	~10	~5	[94]
$Ni_{0.4}Cu_{0.2}Zn_{0.4}Fe_{1.84}Sn_{0.12}O_4$	~11	~10	~10	~5	[94]
$Zn_{0.5}Ni_{0.5}Fe_2O_4$	~200	~50	~7	~1	[95]
$Zn_{0.6}Mn_{0.4}Fe_2O_4$	~50	~50	~8	~1	[96]
$Ni_{0.2}Zn_{0.4}Mn_{0.4}Fe_2O_4$	~50	~50	~6	~1	[96]
$Ni_{0.4}Zn_{0.2}Mn_{0.4}Fe_2O_4$	~250	~50	~4	~1	[96]
$CoFe_2O_4$	~30 - 800	~10 - 130	~1 - 3	~1	[97]
$Ni_{0.43\text{-}x}Cu_xZn_{0.60}Fe_{1.94}O_{3.94}$ (x = 0.10, 0.12, 0.14, 0.16)	–	~15.45–16.15	–	~0.0025	[98]
$BeAl_2O_4$	–	~9.43	–	~0.0005	[99]
$SiMg_2O_4$	–	~6.86	–	~0.0006	[99]
$MgAl_2O_4$	–	~81.8	–	~0.0005	[99]
$SiBe_2O_4$	–	~6.28	–	~0.01	[99]
(MgCoNiCuZn)O	479.07	28.31	7.17	0.62	[100]
$(Co_{0.2}Fe_{0.2}Ni_{0.2}Al_{0.2}Ti_{0.2})_3O_4$ (sintered at 1100 °C)	223	39	1.13	0.13	Present study
$(Co_{0.2}Fe_{0.2}Ni_{0.2}Al_{0.2}Ti_{0.2})_3O_4$ (sintered at 1250 °C)	61	44	0.22	0.01	Present study

temperature are of about 10^2 S cm^{-1} (10^4 S m^{-1}), several orders of magnitude above the scales (10^{-6} to 10^{-4} S m^{-1}) encountered in our high entropy spinels. It hints that other charge carriers are responsible for the observed behavior. Also, due to the frequency range used in our measurements, we wouldn't expect highly mobile carriers, such as electrons, to control the space-charge polarization/relaxation processes in such low frequencies. For instance, the electron hopping frequency in Fe_3O_4 is calculated to be 10^{10}–10^{12} Hz [102], way above typical measurement frequencies via impedance spectroscopy. Because of that, we speculate that ions are the charge carrier species that dominate the electrical behavior in our HEO samples. Even though it is not common to make this attribution, it must be considered that small ions such as Li^+, Na^+, and Mg^{2+} can be transported in the structure of ferrite-based spinels [103–105]. Obviously, with present data, it is not possible to infer which ion(s) would be transported, but it is interesting, for example, that Ni^{2+} and Co^{2+} ionic radii are 69 and 72 p.m. (CN = 4), in the range of the formerly mentioned cations, of respectively 73, 113, and 71 p.m. [106], suggesting that these cations could also be transported and account for the measured conductivities.

We performed impedance spectroscopy data fitting with equivalent circuit models to gain further insights into the electrical behavior of the studied spinel HEOs. Space-charge polarization/relaxation processes are modeled with parallel combinations of resistors and capacitors. Now, the Z' and Z'' spectra shown in Fig. 6 suggest that there are no two regions with different average relaxation times, indicating that a single, long-range, relaxation process dominates the behavior, with a characteristic relaxation frequency below the measured range since a Z'' peak is not observed in any of the samples.

With the intrinsic characteristic of high entropy and local non-uniformity, it is expected that space-charge polarization/relaxation processes will occur over a distribution of frequencies. Given these observations, a possible circuit model to describe the experimental data is composed of a parallel association of a resistor R, a capacitor C, and a *CPE*, a non-ideal element to account for the distribution of relaxation times [107]. Unfortunately, due to the inexistence of Z peaks in the studied frequency, the fits using the complex impedance are not reliable to simultaneously obtain the intrinsic dielectric permittivity (ε_∞) from C and the dc conductivity (σ_{dc}) from R. To do so, we opted to quantify the properties using the combination of ε' and σ spectra. Detailed derivations and mathematical analysis of the set of needed equations can be found elsewhere [108]. In brief, the complex impedance for the resistor, capacitor and CPE are $Z_R^* = R$, $Z_C^* = 1/i\omega C$, and $Z_{CPE}^* = 1/\ K(i\omega)^m$, respectively, where K and m are empirical parameters and $\omega = 2\pi f$. Then, for the $R|C|CPE$ circuit, we have

$$\frac{1}{Z^*} = \frac{1}{R} + i\omega C + K(i\omega)^m = Y^* = G + iB$$

where Y^* is the complex admittance. Using the identity $i^m = \cos(m\pi/2) + i\sin(m\pi/2)$, it leads to

$$Y^* = \frac{1 + RK\omega^m \cos\theta + i(\omega CR + RK\omega^m \sin\theta)}{R}$$

where $\theta = m\pi/2$. By comparing the above equation with $Y^* = G + iB$, it follows that

$$G = \frac{1 + RK\omega^m \cos\theta}{R}$$

$$B = \omega C + K\omega^m \sin\theta$$

Given that the frequency-dependent conductivity and dielectric permittivity are respectively given by $\sigma = GL/A$ and $\varepsilon' = B/\omega C_0$, where $C_0 = \varepsilon_0 L/A$ is the geometric capacitance of free space and ε_0 is the permittivity of free space, it follows that

$$\sigma = \frac{L}{AR} + \frac{L}{A}K\omega^m \cos\theta = \sigma_{dc} + K'\omega^m \cos\left(\frac{m\pi}{2}\right) \tag{12}$$

$$\varepsilon' = \frac{C}{C_0} + \frac{K\sin\theta}{\omega^{1-m}C_0} = \varepsilon_\infty + \frac{K'}{\omega^{1-m}\varepsilon_0}\sin\left(\frac{m\pi}{2}\right) \tag{13}$$

where $K' = KL/A$ and σ_{dc} and ε_∞ are the relevant intrinsic properties of the materials. Finally, equations (12) and (13) are used to fit the frequency-dependent conductivity and dielectric permittivity data, shown in Fig. 7.

With the results in hand, two conclusions can be drawn. First, the intrinsic dielectric permittivity increases with the increase in sintering temperature. This effect should not be related to electronic polarization since both samples have the same composition. On the other hand, the homogenization and greater regularity of the bond distances should facilitate the ionic polarization in the sample sintered at 1250 °C, leading to an overall slight increase in the dielectric permittivity. However, there is an immense decrease in the dc conductivity with the sintering temperature. If, from the applied perspective, it is a nice result because losses will be lower, as observed from the dielectric loss and loss tangent, phenomenologically, this is an intriguing result. In typical electro-ceramics, materials with larger grains tend to have higher conductivities because there are fewer grain boundaries, which usually have higher resistivity and provide a barrier for migrating ions. With the opposite trend here, a speculative explanation lies in the defects created

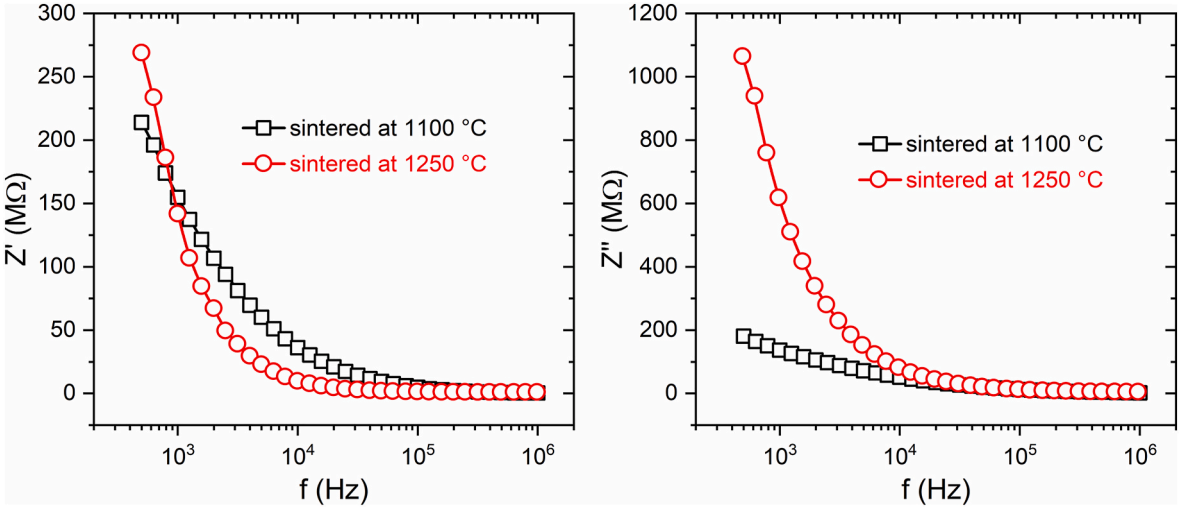

Fig. 6. Variation of real (Z') and imaginary (Z'') components of complex impedance with frequency for different temperature sintered spinel HEOs.

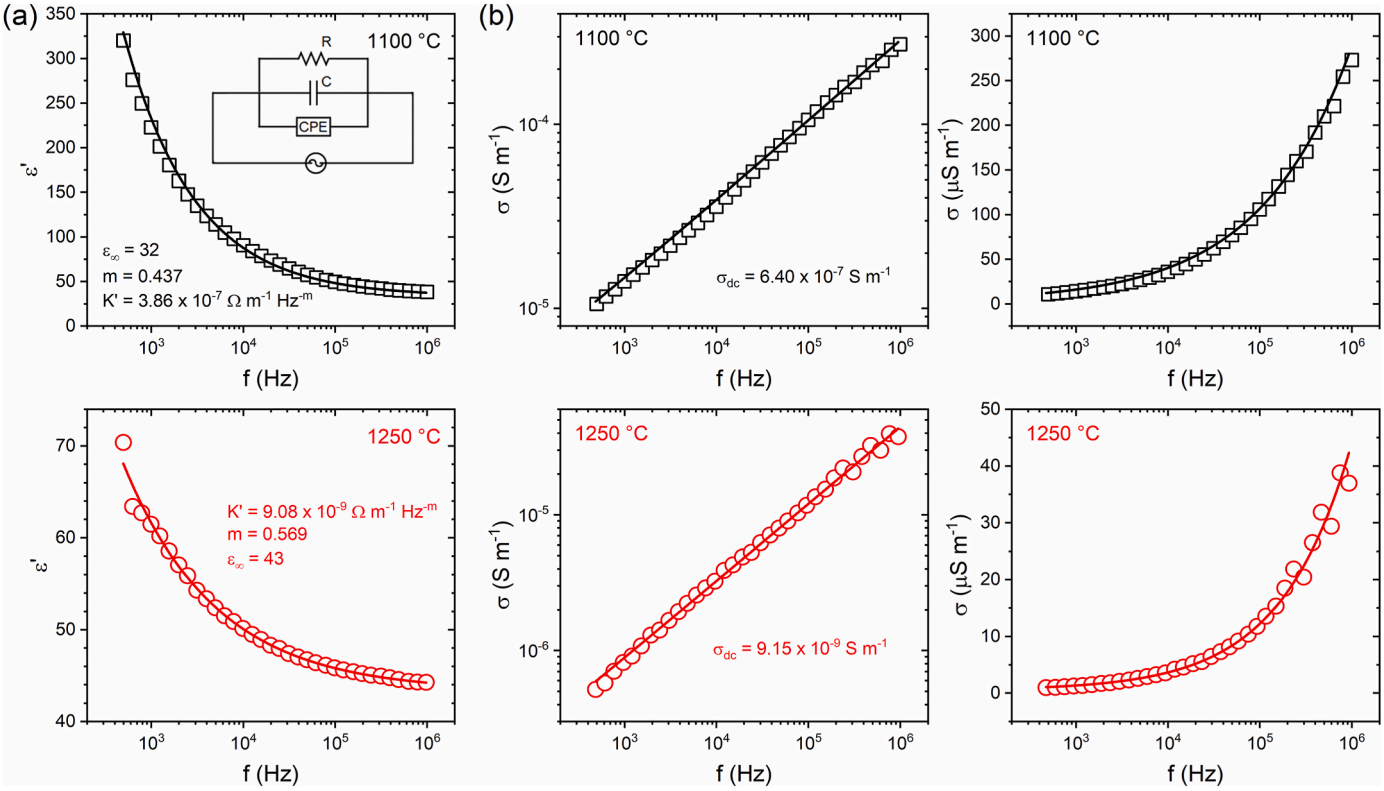

Fig. 7. Fits (lines) of the (a) dielectric permittivity, and (b) conductivity on log and linear scales for different temperature sintered spinel HEOs. The inset represents the *R*|*C*|*CPE* circuit used to model the experimental data.

during the mechanochemical synthesis being healed during synthesis. Increased diffusivity at a higher temperature enhances the system's likelihood of reaching thermodynamic equilibrium. As ions migrate mainly through the transport of their vacancies in the opposite direction, a condition with fewer defects will present fewer mobile ions and, consequently, lower conductivity. Two facts support this hypothesis: the lower micro-strain and higher *m* parameter of the sample sintered at 1250 °C. Interestingly, the *n* value increases with the sintering temperature, which indicates better uniformity, as expected with the higher energy available for the system to reach its equilibrium state, i.e., the chemical homogeneity. An additional consideration is that the lower micro-strain will increase the activation energies to transport ions/defects since, from thermodynamic principles, the strained regions will be in a higher enthalpy level and energetically closer to the top of the energy barrier for the ion jump. With that in mind, ion migration will be mitigated in less-strained conditions, leading to lower ionic conductivity. This last hypothesis could be tested by performing temperature-dependent impedance spectroscopy measurements and will be investigated in future studies.

4. Conclusion

In summary, structural, microstructural, and dielectric properties of multi-cations-based $(Co_{0.2}Fe_{0.2}Ni_{0.2}Al_{0.2}Ti_{0.2})_3O_4$ HEOs synthesized via solid-state mechanochemical route have been investigated in detail. Structural analysis confirmed that 1000 °C sintered ceramics does not show the solid solution phase formation. However, 1100 °C and 1250 °C sintered oxides confirmed the single cubic spinel phase formation in the multi-cations-based ceramic. The qualitative and quantitative morphological analysis was performed using the fractal theory analysis through the Higuchi algorithm approach on the obtained SEM micrograph. With the increase of sintering temperature (from 1100 °C to 1250 °C), the ferrite structural parameters (hopping length, bond length, etc.) increased gradually, while the average aggregated particle size increased substantially from 0.76 μm to 1.82 μm. Moreover, with the enhancement of sintering temperature from 1100 °C to 1250 °C, fractal analysis displayed a negative correlation between surface complexities and space-filling capacity. This means that the change at any successive time step will be in the opposite direction to that of the previous successive time step. Besides, with the change in sintering temperature, the dielectric behavior of the ceramic changed extensively. The 1100 °C sintered ceramic has shown high frequency-dependent dielectric behavior, whereas the 1250 °C sintered ceramic yields low frequency-dependent dielectric behavior. The change in dielectric properties of the ceramics is associated with decreased fractality and increased grain/aggregate particle sizes with sintering temperature. The 1250 °C sintered HEO exhibits low loss tangent ($\tan\delta = 0.01$) with higher dielectric permittivity ($\varepsilon' = 44$) at high frequency (1 MHz), which could be useful for potential multifunctional and microwave device applications. The fractal and impedance spectroscopic analysis explained the microstructure-dielectric property correlations very well. Moreover, the present work is of fundamental importance because it opens new avenues of research in HECs by exploiting the microstructure and dielectric correlations through the first-time employment of fractal analysis.

CRediT authorship contribution statement

Rajesh K. Mishra: Writing – review & editing, Writing – original draft, Software, Methodology, Investigation, Funding acquisition, Formal analysis, Data curation, Conceptualization. **F.B. Minussi:** Writing – review & editing, Software, Formal analysis, Data curation. **Priyanka Kumari:** Formal analysis, Data curation. **Rohit R. Shahi:** Writing – review & editing, Methodology, Conceptualization. **R.P. Yadav:** Software, Formal analysis, Data curation. **Franziska Emmerling:** Writing – review & editing, Validation, Supervision, Funding acquisition. **E.B. Araújo:** Writing – review & editing, Supervision,

Resources, Conceptualization, Methodology, Project administration.

Declaration of competing interest

The authors declare that they have no known competing financial interests or personal relationships that could have appeared to influence the work reported in this paper.

Acknowledgments

This work was financially supported by the BAM's Adolf Martens Fellowship Program, Fundação de Amparo à Pesquisa do Estado de São Paulo (FAPESP Project: 2017/13769-1), and the Coordenação de Aperfeiçoamento de Pessoal de Nível Superior (CAPES-PRINT Project: 88881.310513/2018-01). Rajesh K. Mishra is grateful for the award of the Adolf Martens Fellowship from BAM Germany. The authors also acknowledge Dr. Kavyashree (MNNIT Allahabad, India) for Fractal analysis help and Mr. Elton José de Souza (UNESP, Brazil) and Mr. Saliwan N. Romeo (BAM, Germany) for their measurement support.

Appendix A. Supplementary data

Supplementary data to this article can be found online at https://doi.org/10.1016/j.ceramint.2025.09.256.

References

[1] S. Schweidler, M. Botros, F. Strauss, Q. Wang, Y. Ma, L. Velasco, G.C. Marques, A. Sarkar, C. Kübel, H. Hahn, T. Brezesinski, B. Breitung, High-entropy materials for energy and electronic applications, Nat. Rev. Mater. 9 (2024) 266–281, https://doi.org/10.1038/s41578-024-00654-5.

[2] J. Ma, T. Liu, W. Ye, Q. He, K. Chen, High-entropy perovskite oxides for energy materials: a review, J. Energy Storage 90 (2024) 111890, https://doi.org/10.1016/j.est.2024.111890.

[3] C. Liu, S. Li, Y. Zheng, M. Xu, H. Su, X. Miao, Y. Liu, Z. Zhou, J. Qi, B. Yang, D. Chen, C.W. Nan, Y.H. Lin, Advances in high entropy oxides: synthesis, structure, properties and beyond, Prog. Mater. Sci. 148 (2025) 101385, https://doi.org/10.1016/j.pmatsci.2024.101385.

[4] P. Kumari, A.K. Gupta, R.K. Mishra, M.S. Ahmad, R.R. Shahi, A comprehensive review: recent progress on magnetic high entropy alloys and oxides, J. Magn. Magn Mater. 554 (2022) 169142, https://doi.org/10.1016/j.jmmm.2022.169142.

[5] V.E.A. Montano, M. Kumar Sharma, R.K. Chaurasia, P. Kumar, J.M. Siqueiros, O. R. Herrera, A recent look at high-entropy ceramics based on doping engineering/technology and the future scope of their novel applications, Mater. Lett. 349 (2023) 134785, https://doi.org/10.1016/j.matlet.2023.134785.

[6] X. Ping, B. Meng, X. Yu, Z. Ma, X. Pan, W. Lin, Structural, mechanical and thermal properties of cubic bixbyite-structured high-entropy oxides, Chem. Eng. J. 464 (2023) 142649, https://doi.org/10.1016/j.cej.2023.142649.

[7] S. Ye, J. Zhu, P. Li, M. Li, N. Yan, H. Wang, Study on microstructure, mechanical properties and thermal performance of single-phase (Ti,Zr,Hf)B2 solid solution, Mater. Today Commun. 34 (2023) 105228, https://doi.org/10.1016/j.mtcomm.2022.105228.

[8] T. Yan, M. Luo, J. Chen, H. Zhu, J. Chai, L. Niu, B. Chen, Y. Zhu, T. Shen, Microstructure and mechanical properties of high entropy (MoTaTiVW)C5 ceramics toughened with silicon carbide whisker, Ceram. Int. 50 (2024) 15840–15847, https://doi.org/10.1016/j.ceramint.2024.02.063.

[9] C.M. Rost, E. Sachet, T. Borman, A. Moballegh, E.C. Dickey, D. Hou, J.L. Jones, S. Curtarolo, J.P. Maria, Entropy-stabilized oxides, Nat. Commun. 6 (2015) 8485, https://doi.org/10.1038/ncomms9485.

[10] D.A. Vinnik, E.A. Trofimov, V.E. Zhivulin, O.V. Zaitseva, S.A. Gudkova, A. Yu Starikov, D.A. Zherebtsov, A.A. Kirsanova, M. Häßner, R. Niew, High-entropy oxide phases with magnetoplumbite structure, Ceram. Int. 45 (2019) 12942–12948, https://doi.org/10.1016/j.ceramint.2019.03.221.

[11] Z. Teng, L. Zhu, Y. Tan, S. Zeng, Y. Xia, Y. Wang, H. Zhang, Synthesis and structures of high-entropy pyrochlore oxides, J. Eur. Ceram. 40 (2020) 1639–1643, https://doi.org/10.1016/j.jeurceramsoc.2019.12.008.

[12] L. Spiridigliozzi, C. Ferone, R. Cioffi, G. Dell'Agli, A simple and effective predictor to design novel fluorite-structured High Entropy Oxides (HEOs), Acta Mater. 202 (2021) 181–189, https://doi.org/10.1016/j.actamat.2020.10.061.

[13] X. Li, S. Gao, W. Ji, H. Yu, Y. Chen, Y. Zhang, B. Wan, H. Ma, X. Ji, Rapid synthesis of high entropy perovskite oxides with oxygen vacancies at high pressure for thermoelectric applications, Ceram. Int. 50 (2024) 15144–15158, https://doi.org/10.1016/j.ceramint.2024.01.433.

[14] Z. Zheng, J. Li, X. Deng, M. Xiong, W. Cai, B. Liang, K. Yang, S. Mei, Synthesis and high-pressure properties of $(Nd_{0.2}Li_{0.2}Ba_{0.2}Sr_{0.2}Ca_{0.2})TiO_3$ high-entropy perovskite, Mater. Today Commun. 41 (2024) 110346, https://doi.org/10.1016/j.mtcomm.2024.110346.

[15] C. Liu, J. Bi L. Xie, X. Gao, L. Meng, Preparation and electrochemical properties of two novel high entropy spinel oxides $(MgTiZnNiFe)_3O_4$ and $(CoTiZnNiFe)_3O_4$ by solid state reaction, Mater. Today Commun. 35 (2023) 106315, https://doi.org/10.1016/j.mtcomm.2023.106315.

[16] B. Yang, Y. Liu, S. Lan, L. Dou, C.W. Nan, Y.H. Lin, High-entropy design for dielectric materials: status, challenges, and beyond, J. Appl. Phys. 133 (2023) 110904, https://doi.org/10.1063/5.0138877.

[17] C. Chen, Y. Yang, D. Chen, Y. Zhang, Y. Meng, Micro-structural and magnetic analysis of spinel high entropy oxides synthesized by two-step pressureless sintering provides insight into high entropy ceramics, Mater. Today Commun. 35 (2023) 106122, https://doi.org/10.1016/j.mtcomm.2023.106122.

[18] Z. Lin, B. Ma, Z. Chen, Y. Zhou, Nanostructured spinel high-entropy oxide $(Fe_{0.2}Mn_{0.2}Co_{0.2}Ni_{0.2}\ Zn_{0.2})_3O_4$ as a potential cathode for solid oxide fuel cells, Ceram. Int. l49 (2023) 23057–23067, https://doi.org/10.1016/j.ceramint.2023.04.131.

[19] A.K. Gupta, P. Kumari, A. Prakash, N.K. Giri, R.R. Shahi, Synthesis, characterizations, and magnetic behavior of novel $(CuNiTiZnFe)_3O_4$ high entropy spinel oxide, Ceram. Int. 48 (2022) 36258–36263, https://doi.org/10.1016/j.ceramint.2022.08.183.

[20] Y. He, L. Zhang, H. Xiong, B. Liu, X. Kang, A. Tricoli, Enhanced thermal stability and corrosion resistance of novel high-entropy spinels in cryolite-alumina molten salt applications, Ceram. Int. (2024), https://doi.org/10.1016/j.ceramint.2024.10.075.

[21] A.K. Gupta, K. Shubham, N.K. Giri, R.R. Shahi, Electrochemical charge storage properties of novel inverse spinel $(CuNiZnAlFe)_3O_4$ type high entropy oxide, Energy Storage 6 (2024) e527, https://doi.org/10.1002/est2.527.

[22] A.K. Gupta, A. Singh, P. Kumari, N.K. Giri, R.R. Shahi, Effect of synthesis routes on electrochemical properties as supercapacitor electrode for novel spinel $(CuNiFeMnCo)_3O_4$ high entropy oxide, Energy Storage 6 (2024) e538, https://doi.org/10.1002/est2.538.

[23] A.K. Jha, A.K. Gupta, P. Kumari, R. R Shahi, Dielectric properties of dual phase (Cu-Zn-Ni-Mg-Fe)O high entropy oxide, Indian J. Pure Appl. Phys. 62 (2024) 133–143, https://doi.org/10.56042/ijpap.v62i2.7694.

[24] J. Ma, B. Zhao, H. Xiang, F.Z. Dai, Y. Liu, R. Zhang, Y. Zhou, High-entropy spinel ferrites MFe_2O_4 (M = Mg, Mn, Fe, Co, Ni, Cu, Zn) with tunable electromagnetic properties and strong microwave absorption, J. Adv. Ceram. 11 (2022) 754–768, https://doi.org/10.1007/s40145-022-0569-3.

[25] A. Radoń, Ł. Hawełek, D. Łukowiec, J. Kubacki, P. Włodarczyk, Dielectric and electromagnetic interference shielding properties of high entropy (Zn,Fe,Ni,Mg,Cd)Fe_2O_4 ferrite, Sci. Rep. 9 (2019) 20078, https://doi.org/10.1038/s41598-019-56586-6.

[26] Z. Zheng, B. Liang, J. Gao, J. Ren, Z. Liu, X. Hou, J. Sun, S. Mei, Dielectric properties of $(FeCoCrMnZn)_3O_4$ high-entropy oxide at high pressure, Ceram. Int. 49 (2023) 32521–33252, https://doi.org/10.1016/j.ceramint.2023.07.215.

[27] S. Supriya, $Bi_4Ti_3O_{12}$ electroceramics: effect of doping, crystal structure mechanisms and piezoelectric response, J. Korean Ceram. Soc. 60 (2023) 451–461, https://doi.org/10.1007/s43207-023-00290-9.

[28] S.S. Ryu, S.K. Lee, D.H. Yoon, Synthesis of fine Ca-doped $BaTiO_3$ powders by solid-state reaction method—Part I: mechanical activation of starting materials, J. Electroceram. 18 (2007) 243–250, https://doi.org/10.1007/s10832-007-9066-x.

[29] L. Singh, L. Dhavala, R. Bhimireddi, A.A. Ansari, S. Kumar, V. Srivastava, R. N. Rai, Q.V. Le, Y. Lee, Low-cost flame synthesized $La_{2/3}Cu_3Ti_4O_{12}$ electro-ceramic and extensive investigation on electrical, impedance, modulus, and optical properties, Ceram. Int. l49 (2023) 21795–21803, https://doi.org/10.1016/j.ceramint.2023.04.001.

[30] J.L. Do, T. Friščic, Mechanochemistry: a force of synthesis, ACS Cent. Sci. 3 (2017) 13–19, https://doi.org/10.1021/acscentsci.6b00277.

[31] L. Singh, M. Sheeraz, M.N. Chowdhury, U.S. Rai, S.S. Yadava, Y.S. Park, S.V. Singh Y. Lee, Investigation of dielectric, mechanical, and electrical properties of flame synthesized $Y_{2/3}Cu_{2.90}Zn_{0.10}Ti_4O_{12}$ material, J. Mater. Sci. Mater. Electron. 29 (2018) 10082–10091, https://doi.org/10.1007/s10854-018-9052-x.

[32] J. Dabrowa, M. Stygar, A. Mikuła, Arkadiusz Knapik, K. Mroczka, W. Tejchman, M. Danielewski, M. Martin, Synthesis and microstructure of the (Co,Cr,Fe,Mn,Ni)$_3O_4$ high entropy oxide characterized by spinel structure, Mater. Lett. 216 (2018) 32–36, https://doi.org/10.1016/j.matlet.2017.12.148.

[33] A. Mao, F. Quan, H.Z. Xiang, Z.G. Zhang, K. Kuramoto, A.L. Xia, Facile synthesis and ferrimagnetic property of spinel $(CoCrFeMnNi)_3O_4$ high-entropy oxide nanocrystalline powder, J. Mol. Struct. 1194 (2019) 11–18, https://doi.org/10.1016/j.molstruc.2019.05.073.

[34] X. Sun, X. Zeng, X. He, W. Fang, X. Du, W. Li, L. Zhao, H. Chen, Influence of oxygen vacancies on the structure and magnetic properties of high entropy (Co,Cr,Fe,Mn,Ni)$_3O_4$ ceramics, J. Alloys Compd. 925 (2022) 166560, https://doi.org/10.1016/j.jallcom.2022.166560.

[35] B. Talluri, K. Yoob, J. Kim, High entropy spinel metal oxide $(CoCrFeMnNi)_3O_4$ nanoparticles as novel efficient electrocatalyst for methanol oxidation and oxygen evolution reactions, J. Environ. Chem. Eng. 10 (2022) 106932, https://doi.org/10.1016/j.jece.2021.106932.

[36] C.Q. Duan, K. Tiaa, X. Li, D. Wang, H. Sun, R. Zheng, Z. Wang, Y. Liu, New spinel high-entropy oxides $(FeCoNiCrMnXLi)_3O_4$ (X=Cu, Mg, Zn) as the anode material for lithium-ion batteries, Ceram. Int. 47 (2021) 32025–32032, https://doi.org/10.1016/j.ceramint.2021.08.091.

[37] R.K. Mishra, C.S. Prajapati, P.P. Sahay, Supercapacitive performance of electrochemically synthesized nanocrystalline MnO_2 films using different plating solutions: a comparative study, J. Alloys Compd. 749 (2018) 172–179, https://doi.org/10.1016/j.jallcom.2018.03.271.

[38] R.K. Mishra, C.S. Prajapati, R.R. Shahi, A.K. Kushwaha, P.P. Sahay, Influence of electrodeposition modes on the electrochemical performance of MnO_2 films prepared using anionic $MnO_4{-}(Mn^{7+})$ precursor, Ceram. Int. 44 (2018) 5710–5718, https://doi.org/10.1016/j.ceramint.2017.12.224.

[39] C. Kaushiga, J. Kaarthik, G. Sradha, N. Ram, S.G. Reddy, V. Annapureddy, Influence of sintering temperature strategy on structural, dielectric, and resistive switching in bulk $Ba_{0.7}Sr_{0.3}TiO_3$ ceramic, J. Electron. Mater. 52 (2023) 1691–1699, https://doi.org/10.1007/s11664-022-10119-6.

[40] C. Pithan, H.Y. Lee, M.Y. Yeh, Y.C. Lee, D.F. Hennings, Microstructural and dielectric properties of $Ba_{0.45}Mg_{0.05}Sr_{0.5-x}Ca_xTiO_3$ high entropy ceramics, Mater. Chem. Phys. 296 (2023) 127290, https://doi.org/10.1016/j.matchemphys.2022.127290.

[41] R.K. Mishra, R.R. Shahi, Phase evolution and magnetic characteristics of TiFeNiCr and TiFeNiCrM (M = Mn, Co) high entropy alloys, J. Magn. Magn Mater. 442 (2017) 218–223, https://doi.org/10.1016/j.jmmm.2017.06.124.

[42] R.P. Yadav Kavyashree, S. Parveen, L.P. Joshi, S.N. Pandey, Fractal characterization of flakes covered tuberose structured $Cu:Sr(OH)_2$ thin film as supercapacitive electrode, Mater. Res. Bull. 120 (2019) 110574, https://doi.org/10.1016/j.materresbull.2019.110574.

[43] Kavyashree, R.K. Pandey, R.P. Yadav, M. Kumar, H.P. Bhasker, A.K. Mittal, A. C. Pandey, S.N. Pandey, Substrate effect on the evolution of surface morphology of BaF_2 thin films: a study based on fractal concepts, Appl. Surf. Sci. 466 (2019) 780–786, https://doi.org/10.1016/j.apsusc.2018.10.075.

[44] C. Kumar Vinita, R.P. Yadav, B.K. Singh, Surfaces properties correlation with optical parameters of thickness dependent self-affine nanostructured SnS thin films: a study based on scaling law, Colloids Surf., A: Physicochem. Eng. 691 (2024) 133865, https://doi.org/10.1016/j.colsurfa.2024.133865.

[45] Z.Z. Lazarevic, C. Jovalekic, A. Milutinovic, D. Sekulic, V.N. Ivanovski, A. Recnik, B. Cekic, N.Z. Romcevic, Nanodimensional spinel $NiFe_2O_4$ and $ZnFe_2O_4$ ferrites prepared by soft mechanochemical synthesis, J. Appl. Phys. 113 (2013) 187221, https://doi.org/10.1063/1.4801962.

[46] D.K. Pradhan, P. Misra, V.S. Puli, S. Sahoo, D.K. Pradhan, R.S. Katiyar, Studies on structural, dielectric, and transport properties of $Ni_{0.65}Zn_{0.35}Fe_2O_4$, J. Appl. Phys. 115 (2014) 243904, https://doi.org/10.1063/1.4885420.

[47] X. Xu, J.H. Kim, W.K. Yeoh, Y. Zhang, S.X. Dou, Improved Jc of MgB_2 superconductor by ball milling using different media, Supercond. Sci. Technol. 19 (2006) L47–L50, https://doi.org/10.1088/0953-2048/19/11/L01.

[48] H. Kurama, Ş. Erkuş, H. Gaşan, The effect of process control agent usage on the structural properties of MgB_2 synthesized by high energy ball mill, Ceram. Int. 43 (2017), https://doi.org/10.1016/j.ceramint.2017.05.274. S391-S-396.

[49] L. Lu, M.O. Lai, S. Zhang, Diffusion in mechanical alloying, J. Mater. Process. Technol. 67 (1997) 100–104, https://doi.org/10.1016/S0924-0136(96)02826-9.

[50] Z. Cvejic, E. ĐurCic, G.I. Ivandekic, B. Bajac, P. Postolache, L. Mitoseriu, V. V. Srdic, S. Rakic, The effect of annealing on microstructure and cation distribution of $NiFe_2O_4$, J. Alloys Compd. 649 (2015) 1231–1238, https://doi.org/10.1016/j.jallcom.2015.07.238.

[51] R. Roongtao, C. Ruttanapun, Influence of change in cation distribution on the magnetic and catalytic properties via thermal annealing of spinel-type $CoFe_2O_4$, Jpn. J. Appl. Phys. 58 (2019) 101001, https://doi.org/10.7567/1347-4065/ab3bef.

[52] A. Ahlawat, V.G. Sathe, Raman study of $NiFe_2O_4$ nanoparticles, bulk and films: effect of laser power, J. Raman Spectrosc. 42 (2011) 1087–1094, https://doi.org/10.1002/jrs.2791.

[53] C. Cherpin, D. Lister, F. Dacquait, L. Liu, Study of the solid-state synthesis of nickel ferrite ($NiFe_2O_4$) by X-ray diffraction (XRD), scanning electron microscopy (SEM) and Raman spectroscopy, Materials 14 (2021) 2557, https://doi.org/10.3390/ma14102557.

[54] R. Tiwari, M. De, H.S. Tewari, S.K. Ghoshal, Structural and magnetic properties of tailored $NiFe_2O_4$ nanostructures synthesized using auto-combustion method, Results Phys. 16 (2020) 102916, https://doi.org/10.1016/j.rinp.2019.102916.

[55] P. Kumari, A. Kumar, R.K. Mishra, S.K. Mohapatra, A.K. Gupta, M.A. Shaz, T. P. Yadav, R.R. Shahi, Investigations on phase formation and magnetic properties of promising $Co_{35}Cr_5Fe_{10}Ni_{30}Ti_{20}$ high entropy alloy synthesized through radio frequency induction melting, J. Alloys Compd. 960 (2023) 170697, https://doi.org/10.1016/j.jallcom.2023.170697.

[56] D.S. Nikam, S.V. Jadhav, V.M. Khot, R.A. Bohara, C.K. Hong, S.S. Malib, S. H. Pawar, Cation distribution, structural, morphological and magnetic properties of $Co_{1-x}Zn_xFe_2O_4$ (x = 0 – 1) nanoparticles, RSC Adv. 5 (2015) 2338–2345, https://doi.org/10.1039/C4RA08342C.

[57] S.M. Kabbur, U.R. Ghodake, D.Y. Nadargi, Rahul C. Kambale, S.S. Suryavanshi, Effect of Dy^{3+} substitution on structural and magnetic properties of nanocrystalline ni-cu-zn ferrites, J. Magn. Magn Mater. 451 (2018) 665–675, https://doi.org/10.1016/j.jmmm.2017.12.006.

[58] A. Diallo, A.C. Beye, T.B. Doyle, E. Park, M. Maaza, Green synthesis of Co_3O_4 nanoparticles via Aspalathus linearis: physical properties, Green Chem. Lett. Rev. 8 (2015) 30–36, https://doi.org/10.1080/17518253.2015.1082646.

[59] Z.Z. Lazarevic, C. Jovalekic, D.L. Sekulic, A. Milutinovic, S. Balos, M. Slankamenac, N.Z. Romcevic, Structural, electrical and dielectric properties of spinel nickel ferrite prepared by soft mechanochemical synthesis, Mater. Res. Bull. 48 (2013) 4368–4378, https://doi.org/10.1016/j.materresbull.2013.07.012.

[60] P.R. Kumar, Y.H. Jung, K.K. Bharathi, C.H. Lim, D.K. Kim, High capacity and low cost spinel Fe_3O_4 for the Na-ion battery negative electrode materials, Electrochim. Acta 146 (2014) 503–510, https://doi.org/10.1016/j.electacta.2014.09.081.

[61] S.J.L. Kang, Sintering: Densification, Grain Growth & Microstructure, first ed., Elsevier Butterworth-Heinemann, Londaon, 2005.

[62] D. Chaira, Powder metallurgy routes for composite materials production, Encycloped. Mater.: Composit. 2 (2021) 588–604, https://doi.org/10.1016/B978-0-12-803581-8.11703-5.

[63] M.R. Mazlan, N.H. Jamadon, A. Rajabi, A.B. Sulong, I.F. Mohamed, F. Yusof, N. A. Jama, Necking mechanism under various sintering process parameters: a review, J. Mater. Res. Technol. 23 (2023) 2189–2201, https://doi.org/10.1016/j.jmrt.2023.01.013.

[64] V. Mitic, G. Lazovic, V. Paunovic, J.R. Hwu, S.C. Tsay, T.P. Perng, S. Veljkovic, B. Vlahovic, Ceramic materials and energy—Extended Coble's model and fractal nature, J. Eur. Ceram. Soc. 39 (2019) 3513–3525, https://doi.org/10.1016/j.jeurceramsoc.2019.04.009.

[65] L.C. Dufour, C. Monty, G.P. Ervas, Surfaces and Interfaces of Ceramic Materials, first ed., Kluwer Academic Publishers, London, 1989.

[66] K. Catalbas, N.K. Gozuacik, N. Basaran, N.T. Selli, E. Mensur, Mechanical and dielectric properties of MgO ceramics with HNT additions, J. Australas. Ceram. Soc. (2025), https://doi.org/10.1007/s41779-024-01145-0.

[67] Y. Liu, G. He, Y. Nie, W. Zhang, Z. Zhao, H. Zhou, Influence of sintering characteristics and structural properties on the microwave dielectric properties of non-stoichiometric $Ca3Mn2{+}xGe3O12{+}\delta$ (x =0–0.2) ceramics, J. Mater. Chem. C 12 (2024) 6615–6627, https://doi.org/10.1039/D4TC00698D.

[68] J. Zhang D.Y. Xu, L. Tong, H.C. Qi, D.L. Zhang, C.C. Wang, Surface layer and its effect on dielectric properties of SiC ceramics, J. Alloys Compd. 734 (2018) 16–21, https://doi.org/10.1016/j.jallcom.2017.10.218.

[69] J. Zhao, R. Zhu, Q. Du, F. Liu, Y. Wu, D. Lin, H. Xu, W. Di, J. Chen, H. Luo, Surface and thickness effect on the ferroelectric, dielectric and pyroelectric properties of Mn-doped $Pb(Mg_{1/3}Nb_{2/3})O_3$-$0.28PbTiO_3$ single crystals, J. Alloys Compd. 816 (2020) 152500, https://doi.org/10.1016/j.jallcom.2019.152500.

[70] Y.R. Barcelay, A.S. Silva, R.S. Matos, A. Das, S. Kumar, R.P. Yadav, A. Gandarilla, W.R. Brito, H.D.F. Filho, Tailoring the surface topography and crystallinity of $EuMnO_3$ films: a study on sintering effects, Surf. Interfaces 52 (2024) 104829, https://doi.org/10.1016/j.surfin.2024.104829.

[71] S. Aman, M.B. Tahir, N. Ahmad, The enhanced electrical and dielectric properties of cobalt-based spinel ferrites for high-frequency applications, J. Mater. Sci. Mater. Electron. 32 (2021) 22440–22449, https://doi.org/10.1007/s10854-021-06730-8.

[72] S.B. Kale, R.M. Borade, J.S. Kounsalye, A.V. Raut, S.R. Nimbhore, K.M. Jadhav, Structural and dielectric properties of mixed spinel ferrite $Cu_{(0.7)}Zn_{(0.3)}Fe_2O_4$ nanoparticles, J. Phys.: Conf. Ser. 1644 (2020) 012012, https://doi.org/10.1088/1742-6596/1644/1/012012.

[73] H.P.P.V. Shanmugasundram, E. Jayamani, K.H. Soon, A comprehensive review on dielectric composites: classification of dielectric composites, Renew. Sust. Energ. 157 (2022) 112075, https://doi.org/10.1016/j.rser.2022.112075.

[74] Y. Wang, Y. Tan, H. Wang, Y. Cen, J. Ma, Q. Ruan, L. Wang, J. Cai, The relationship between the defect structure and dielectric properties of (La, Li) co-doped $SrTiO_3$, J. Mater. Sci. Mater. Electron. 35 (2024) 1058, https://doi.org/10.1007/s10854-024-12813-z.

[75] W. Hu, Y. Liu, R.L. Withers, T.J. Frankcombe, L. Norén, A. Snashall, M. Kitchin, P. Smith, B. Gong, H. Chen, J. Schiemer, F. Brink, J.W. Leung, Electron-pinned defect-dipoles for high-performance colossal permittivity materials, Nature Mater 12 (2013) 821–826, https://doi.org/10.1038/nmat3691.

[76] J. Qi, M. Cao, Y. Chen, Y. Fang, W. Pan, H. Hao, Z. Yao, Z. Yu, H. Liu, Effects of sintering temperature on microstructure and dielectric properties of $Sr_{0.985}Ce_{0.01}TiO_3$ ceramics, J. Alloys Compd. 762 (2018) 950–956, https://doi.org/10.1016/j.jallcom.2018.05.140.

[77] W. Tuichai, S. Danwittayakul, N. Chanlek, P. Thongbai, Effects of sintering temperature on microstructure and giant dielectric properties of (V + Ta) co-doped TiO_2 ceramics, J. Allpys Compd. 725 (2017) 310–317, https://doi.org/10.1016/j.jallcom.2017.07.143.

[78] V.R. Mudinepalli, L. Feng, W.C. Lin, B.S. Murty, Effect of grain size on dielectric and ferroelectric properties of nanostructured $Ba_{0.8}Sr_{0.2}TiO_3$ ceramics, J. Adv. Ceram. 4 (2015) 46–53, https://doi.org/10.1007/s40145-015-0130-8.

[79] Y. Huang, Y. Wang, Z. Li, Z. Yang, C. Shen, C. He, Effect of pore morphology on the dielectric properties of porous carbons for microwave absorption applications, J. Phys. Chem. C 118 (2014) 26027–26032, https://doi.org/10.1021/jp506999k.

[80] D. Xiao, L. Meng, G. Yu, The effect of surface layer on the dielectric behavior of complex oxide thin films, Mater. Des. 24 (2003) 377–382, https://doi.org/10.1016/S0261-3069(03)00030-X.

[81] J. Shi, K. Ao, I. Firdous, X. Zhang, M. Fahim, L. Wang, W.A. Daoud, Dynamic quantification of the overall effect of dielectric polarization, Nano Energy 105 (2023) 108029, https://doi.org/10.1016/j.nanoen.2022.108029.

[82] Y.G. Abreu, S.P. Reis, F.E. Freitas, J.A. Eiras, E.B. Araújo, Effects of crystallization kinetics on the dielectric and electrical properties of $BiFeO_3$ films, J. Adv. Dielect. 11 (2021) 2140007, https://doi.org/10.1142/S2010135X21400075.

[83] N. Rezlescu, E. Rezlesc, Dielectric properties of copper containing ferrites, Phys. Stat. Sol. (A) 23 (1974) 575–582, https://doi.org/10.1002/pssa.2210230229.

[84] D. Ravinder, S. Ramana Murthy, V.N. Mulay, K.B. Reddy, Low-frequency dielectric behaviour of lithium–zinc ferrites, Phys. Stat. Sol. (A) 134 (1992) 273–278, https://doi.org/10.1002/pssa.2211340124.

[85] D. Ravinder, Dielectric behaviour of lithium-cadmium ferrites, Phys. Stat. Sol. (A) 129 (1992) 549–554, https://doi.org/10.1002/pssa.2211290225.

[86] O.S. Josyulu, J. Sobhanadri, DC conductivity and dielectric behaviour of cobalt-zinc ferrites, Phys. Stat. Sol. (A) 59 (1980) 323–329, https://doi.org/10.1002/pssa.2210590143.

[87] K. Latha, K. Satya Mohan, D. Ravinder, Dielectric behaviour of mixed Mn-Zn ferrites, Phys. Stat. Sol. (A) 142 (1994) K103–K106, https://doi.org/10.1002/pssa.2211420240.
[88] M.A. Ahmed, M.K. El-nimr, A. Tawfik, A.M. Aboelata, Dielectric behaviour in Co-Zn ferrites, Phys. Stat. Sol. (A) 114 (1989) 377–380, https://doi.org/10.1002/pssa.2211140139.
[89] S. Anjum, A. Rashid, F. Bashir, S. Riaz, M. Pervaiz, R. Zia, Effect of Cu-Doped nickel ferrites on structural, magnetic, and dielectric properties, Mater. Today Proc. 2 (2015) 5559–5567, https://doi.org/10.1016/j.matpr.2015.11.086.
[90] A.A. Bush, V. Ya Shkuratov, K.E. Kamentsev, A.S. Prokhorov, E.S. Zhukova, B. P. Gorshunov, V.I. Torgashev, Ferroelectricity in spinel solid solution $Co_{0.8}Ni_{0.2}Cr_2O_4$, Phy. Rev. B 85 (2012) 214112, https://doi.org/10.1103/PhysRevB.85.214112.
[91] S. Aman, M. Bilal Tahir, N. Ahmad, The enhanced electrical and dielectric properties of cobalt-based spinel ferrites for high-frequency applications, J. Mater. Sci. Mater. Electron. 32 (2021) 22440–22449, https://doi.org/10.1007/s10854-021-06730-8.
[92] S.B. Kale, R.M. Borade, J.S. Kounsalye, A.V. Raut, S.R. Nimbhore, K.M. Jadhav, Structural and dielectric properties of mixed spinel ferrite $Cu_{(0.7)}Zn_{(0.3)}Fe_2O_4$ nanoparticles, J. Phys.: Conf. Ser. 1644 (2020) 012012, https://doi.org/10.1088/1742-6596/1644/1/012012.
[93] D. Ravinder, K. Latha, Dielectric behaviour of mixed Mg–Zn ferrites at low frequencies, Mater. Lett. 41 (1999) 247–253, https://doi.org/10.1016/S0167-577X(99)00138-X.
[94] B. Ünal, M.A. Almessiere, A. Baykald, Y. Slimani, M.A. Gondal, N. Kian-Pourg, S. E. Shirsathh, A. Manikandani, U. Baig, Comprehensive analysis of $Ni_{0.4}Cu_{0.2}Zn_{0.4}Fe_{2-4x}$ $Sn_{3x}O_4$ nano spinel ferrites: structural, electrical, and dielectric characterization through advanced techniques, Ceram. Int. 50 (2024) 30670–30682, https://doi.org/10.1016/j.ceramint.2024.05.367.
[95] M.E. Hajlaoui, R. Dhahri, N. Hnainia, A. Benchaabane, E. Dhahri, K. Khirouni, Conductivity and giant permittivity study of Zn0.5Ni0.5Fe2O4 spinel ferrite as a function of frequency and temperature, RSC Adv. 9 (2019) 32395–32402, https://doi.org/10.1039/C9RA06589J.
[96] Md Suzauddulah, M.K.R. Khan, F.A. Khan, M.M. Rahman, M.S.I. Sarker, Structural, morphological and frequency dependent dielectric properties of $Ni_xZn_{0.6-x}Mn_{0.4}Fe_2O_4$ ($0.0 \leq x \leq 0.4$) nanoparticles prepared by sol-gel method, Mater. Chem. Phy. 304 (2023) 127866, https://doi.org/10.1016/j.matchemphys.2023.127866.
[97] R. Zhang, L. Sun, Z. Wang, W. Hao, E. Cao, Y. Zhang, Dielectric and magnetic properties of $CoFe_2O_4$prepared by sol-gel auto-combustion method, Mater. Res. Bull. 98 (2018) 133–138, https://doi.org/10.1016/j.materresbull.2017.08.006.
[98] X. Ji, T. Chen, C. Shen, Ye Zhao, K. Zhou, M. Sun, Y. Yu, L. Fan, H. ui Zheng, Q. Wu, Q. Zhang, Yang Zhang, Magnetic and dielectric properties of NiCuZn ferrite with optimized Cu content and sintered by a two-step process, J. Alloys Compd. 898 (2022) 162906, https://doi.org/10.1016/j.jallcom.2021.162906.
[99] R.D. Shannon, M.A. Subramanian, Dielectric constants of chrysoberyl, spinel, phenacite, and forsterite and the oxide additivity rule, phays, Chem. Minerals 16 (1989) 747–751, https://doi.org/10.1007/BF00209696.
[100] H.N. Thenuwara, H.J. Shih, H.L. Senevirathna, Y.C. Lee, X. Li, P. Wu, Electronic structure design in high-entropy oxides: enabling frequency-dependent dielectric behavior for advanced applications, ACS Appl. Electron. Mater. 7 (2025) 831–837, https://doi.org/10.1021/acsaelm.4c01979.
[101] C.B. Carter, M.G. Norton, Ceramic Materials: Science and Engineering, second ed., Springer, New York, 2013.
[102] F.N. Skomurski, S. Kerisit, K.M. Rosso, Structure, charge distribution, and electron hopping dynamics in magnetite (Fe_3O_4) (100) surfaces from first principles, Geochem. Cosmochim. Acta 74 (2010) 4234–4248, https://doi.org/10.1016/j.gca.2010.04.063.
[103] S. Komaba, T. Mikumo, N. Yabuuchi, A. Ogata, H. Yoshida, Y. Yamada, Electrochemical insertion of Li and Na ions into nanocrystalline Fe_3O_4 and α-Fe_2O_3 for rechargeable batteries, J. Electrochem. Soc. 157 (2010) A60, https://doi.org/10.1149/1.3254160.
[104] K.W. Knehr, N.W. Brady, C.A. Cama, D.C. Bock, Z. Lin, C.N. Lininger, A. C. Marschilok, K.J. Takeuchi, E.S. Takeuchi, A.C. West, Modeling the mesoscale transport of lithium-magnetite electrodes using insight from discharge and voltage recovery experiments, J. Electrochem. Soc. 162 (2015) A2817–A2826, https://doi.org/10.1149/2.0961514jes.
[105] H. Ren, H. Li, P. Barry, Z. Wang, A.R. Campos, E.S. Takeuchi, A.C. Marschilok, S. Yan, K.J. Takeuchi, E. Reichmanis, Recent advances in the application of magnetite (Fe_3O_4) in lithium-ion batteries: synthesis, electrochemical performance, and characterization techniques, Chem. Mater. 36 (2024) 9299–9319, https://doi.org/10.1021/acs.chemmater.4c02013.
[106] R.D. Shannon, Revised effective ionic radii and systematic studies of interatomic distances in halides and chalcogenides, Acta Cryst A 32 (1976) 751–767, https://doi.org/10.1107/S0567739476001551.
[107] K.S. Cole, R.H. Cole, Dispersion and absorption in dielectrics I. Alternating current characteristics, J. Chem. Phys. 9 (1941) 341–351, https://doi.org/10.1063/1.1750906.
[108] F.B. Minussi, F.V.A. Borges, E.B. Araújo, Charge transport and dielectric characteristics of $Sm_xBi_{1-x}FeO_3$ thin films from the perspective of grain and grain boundary properties, J. Phys. D Appl. Phys. 56 (2023) 355302, https://doi.org/10.1088/1361-6463/acd791.